

# UNIVERSITY OF TWENTE.

Faculty of Engineering Technology

*Document number: 417*

## Computational modelling of cerebrospinal fluid flow in perivascular spaces

F.W. Schermer  
M.Sc. Thesis  
November 2022

---

**Supervisor:**  
dr. K. Jain

Engineering Fluid Dynamics Group  
Faculty of Engineering Technology  
University of Twente  
P.O. Box 217  
7500 AE Enschede  
The Netherlands

---



# Abstract

The flow of cerebrospinal fluid in the perivascular space is part of the waste clearance system of the brain. This system is responsible for clearing waste proteins, such as amyloid- $\beta$ , produced by the brain. Accumulation of amyloid- $\beta$  is linked to neurological disorders like Alzheimer's disease. Gaining knowledge on the flow of cerebrospinal fluid in these perivascular spaces is therefore crucial. Currently all simulation studies use a concentric shape for the perivascular space, but recent magnetic resonance imaging studies have shown that the perivascular space is more elliptical and the artery is often off-centered. Therefore, in this study several cross-sectional shapes have been used to investigate the effect of this change of shape on the flow of cerebrospinal fluid in the perivascular space.

The simulations in this study are performed using a Lattice Boltzmann Method solver. Three different cross-sectional shapes have been used for the simulations, being a concentric annulus, a flattened annulus and a flattened annulus with an off-centered artery. The fluid simulation showed that local velocities can increase up to 150% for the flattened PVS shape and up to 190% for the flattened PVS shape with an off-centered artery when compared to the concentric PVS. Also, the flow distribution around the artery is changed significantly with the cross-sectional shape, shifting from an evenly distributed flow in the concentric shape to a flow with two dominant regions in the flattened shape and a single dominant flow region in the off-centered shape. The local velocity differences have been shown to reduce around a bifurcation, where a more similar flow distribution is seen between the concentric and the flattened shape. In the cornering regions both flows show a single dominant flow, however the flow in the flattened geometry is forced to a different path due to the twisting of its geometry.

**Keywords:** Lattice Boltzmann Method; Computational Fluid Dynamics; Cerebrospinal Fluid; Perivascular Spaces; Musubi; Alzheimer's Disease;

# Nomenclature

## Abbreviations

<i>BGK</i>	Bhatnagar-Gross-Krook (operator)
<i>BTE</i>	Boltzmann Transport Equation
<i>CFD</i>	Computational Fluid Dynamics
<i>CSF</i>	Cerebrospinal fluid
<i>LBM</i>	Lattice Boltzmann Method
<i>MRI</i>	Magnetic Resonance Imaging
<i>PDE</i>	Partial Differential Equation
<i>PVS</i>	Perivascular space

## Physical parameters

$\mu$	Dynamic viscosity	[Pa · s]
$\nu$	Kinematic viscosity	[m <sup>2</sup> /s]
$\omega$	Collision frequency	[–]
$\rho$	Density	[kg/m <sup>3</sup> ]
$\tau$	Relaxation factor	[–]
$c_s$	Lattice speed of sound	[m/s]
$D_h$	Hydraulic diameter	[m]
$f_{eq}$	Equilibrium distribution function	[–]
$K_b$	Boltzmann constant	[s]
$m$	Mass	[kg]
$N$	Number of elements	[–]
$P$	Pressure	[Pa]
$R_{sp}$	Specific gas constant	[J/(kg · K)]
$T$	Temperature	[K]
$c$	Lattice velocity	[m/s]
$F$	Force	[kg · m/s <sup>2</sup> ]
$f$	Distribution function	[–]
$h$	Grid spacing	[m]
$Ma$	Mach number	[–]
$p$	Momentum	[kg · m/s]
$Re$	Reynolds number	[–]
$t$	Time	[s]
$u$	Velocity	[m/s]

# Contents

<b>1</b>	<b>Introduction</b>	<b>1</b>
1.1	Research question . . . . .	2
1.2	Scope . . . . .	2
1.3	Outline . . . . .	2
<b>2</b>	<b>Biomedical background study</b>	<b>3</b>
2.1	Brain physiology and cerebrospinal fluid . . . . .	3
2.2	Pial arteries and perivascular spaces . . . . .	5
2.3	Cerebrospinal fluid flow in perivascular spaces . . . . .	7
<b>3</b>	<b>Lattice Boltzmann theory</b>	<b>9</b>
3.1	The Boltzmann equation . . . . .	10
3.2	Bhatnagar Gross Krook relaxation . . . . .	12
3.3	Discretization . . . . .	14
3.4	Boundary conditions . . . . .	15
3.4.1	Bounce-back boundary condition . . . . .	15
3.4.2	Dirichlet boundary condition . . . . .	17
3.5	Selection of lattice parameters . . . . .	18
<b>4</b>	<b>Simulation environment</b>	<b>19</b>
4.1	APES software . . . . .	19
4.2	Seeder . . . . .	20
4.3	Musubi . . . . .	21
4.4	Post-processing . . . . .	21
<b>5</b>	<b>Preliminary flow studies</b>	<b>22</b>
5.1	Geometry . . . . .	22
5.2	Analytical solution . . . . .	23
5.3	Simulation results . . . . .	24
5.4	Convergence . . . . .	26
<b>6</b>	<b>Straight artery simulations</b>	<b>27</b>
6.1	CSF fluid and flow . . . . .	27
6.1.1	Cerebrospinal fluid characteristics . . . . .	27
6.1.2	CSF flow in rodents . . . . .	28
6.1.3	CSF flow in humans . . . . .	28
6.2	Geometry and simulation setup . . . . .	30
6.3	Analysis . . . . .	32

---

<b>7</b>	<b>Geometry change effect on previous studies</b>	<b>36</b>
7.1	Details of the research . . . . .	36
7.2	Simulation parameters . . . . .	37
7.3	Analysis . . . . .	39
<b>8</b>	<b>Realistic artery study</b>	<b>43</b>
8.1	Geometry . . . . .	43
8.2	Simulation parameters . . . . .	46
8.3	Analysis . . . . .	46
8.3.1	Velocity profile slices . . . . .	47
8.3.2	Streamline plots . . . . .	50
8.3.3	Glyph plots . . . . .	53
8.3.4	Velocity profiles over time . . . . .	57
<b>9</b>	<b>Discussion, conclusions and recommendations</b>	<b>60</b>
9.1	Discussion . . . . .	60
9.2	Conclusions . . . . .	62
9.3	Recommendations . . . . .	63

# Chapter 1

## Introduction

A major health issue in the current era among elderly people is dementia. Dementia is currently the seventh leading cause of death among all diseases and one of the major causes of disability and dependency among older people worldwide [1]. Currently about 50 million people worldwide suffer from dementia, between 60% and 70% of this group are estimated to have Alzheimer's disease [2]. As such Alzheimer's disease is the most common cause of dementia and the fifth leading cause of death in adults older than 65 year [3]. Alzheimer's disease is a progressive neurological disorder that causes the brain to shrink and brain cells to die. As a result the patient has a continuous decline in thinking, behavioural and social skills and the ability to function independently. The estimated total healthcare costs for the treatment of Alzheimer's disease in 2020 is estimated at 305 billion dollars, with the costs expected to increase to more than 1 trillion dollars as the population ages [3]. These costs are attributed to skilled nursing care, home healthcare and hospice care. Furthermore, dementia causes a significant burden on the patients carers, families and society at large.

With such consequences and costs associated with Alzheimer's disease it is of high importance to be able to correctly assess whether a patient suffers from the disease or not. However currently neurologists do not have the right tools at their disposal for an accurate assessment that could lead to a definitive diagnosis of Alzheimer's Disease. After all, having memory problems can be a symptom of many different cognitive diseases and the current diagnoses based on memory tests are not made until there is significant memory impairment, which makes effective treatment difficult. Therefore, researchers are searching for earlier signs of Alzheimer's disease. This research is currently focused on cerebrospinal fluid (CSF) bio-markers. Research on brain tissue of patients showed an accumulation of toxic forms of the protein amyloid- $\beta$ , which is a waste product of the brain cells [4]. As such the clearance of these waste products has become topic of research.

Inside the brain these proteins are transported via cerebrospinal fluid in the perivascular spaces (PVS) around the arteries which leads to researchers looking into the behaviour of this flow and possible obstruction of this type of flow. In vivo measurements are not an option in human patients, therefore the focus of these studies is on simulation work. There are results of in vivo measurement on mice and rodents, which can be scaled to the human brain equivalent such that representative simulations can be performed. The main point of critique on the current simulation studies however is that all these studies assume a concentric shaped PVS. Recent studies have shown that the shape of the PVS is more flattened, often two-lobed and sometimes eccentric [5]. It is therefore questionable to what extend these simulations offer representative insight in the CSF flow.

In this thesis fluid flow analyses will be performed on cerebrospinal fluid in the brain using several different shapes for the perivascular space. As such an insight is given in the validity of previous performed simulation studies and recommendations for upcoming simulations can be given. The simulations in this thesis will be performed using the Lattice Boltzmann Method (LBM), which is a statistical approach to solve the Boltzmann transport formula. This method is mostly used for complex geometries and as such this method is chosen here since follow up research will result in more complex artery geometries.

## 1.1 Research question

The main research question of this thesis is:

**To what extent does the cross-sectional shape of the PVS influence the fluid behaviour of CSF?**

Next to this several sub questions are answered in this thesis which are:

1. What are valid cross-sectional shapes for the perivascular space?
2. What simplifications of the geometry are valid to make in this case?
3. To what extent are previously performed simulation studies using concentric PVS shapes still valid?

## 1.2 Scope

This thesis focuses on the changes occurring in fluid flow characteristics when using different cross-sectional shapes for the PVS. The results of this research are valuable as feedback to previous performed computational studies, either verifying that using a concentric PVS shape is sufficient, or motivating the use of a different shaped PVS to more accurately represent the real case. Understanding the CSF flow in PVS is vital in the research to combat Alzheimer's disease, as understanding a problem is the first step towards solving it, therefore an accurate representation of the real life scenario has to be a priority.

In this thesis the Lattice Boltzmann Method will be used to perform the simulation. A general understanding of the method is necessary, however it does not have to be used to build a code as a framework package called APES is readily available for the simulations.

## 1.3 Outline

This report will first present the necessary biomedical knowledge required to understand the problem, focusing on the CSF flow, the PVS and the brain physiology in general.

After this the theory of the Lattice Boltzmann Method is explained and some insights into the APES simulation framework are discussed.

Then a grid convergence study is performed on a simple geometry, which also serves as a verification of the Lattice Boltzmann Method and the used simulation framework.

With this setup completed three sets of simulations are presented and discussed which comprise the results of this thesis.

Finally the report ends with the discussion, conclusions and the recommendations for further studies.

## Chapter 2

# Biomedical background study

The application of the research conducted in this thesis is in the medical field and more specifically the brain. To be able to conduct the research in this thesis however a thorough understanding of the brain and its functions is not required, but a basic understanding of the most important concepts has to be included to sufficiently understand the application. As such a literature study is performed in order to understand the concepts of cerebrospinal fluid and its functions, section 2.1, the perivascular space around pial arteries in the brain, section 2.2, and the flow of cerebrospinal fluid through the brain, section 2.3.

### 2.1 Brain physiology and cerebrospinal fluid

The brain is a complex organ that controls every function of the body. Intelligence, creativity, emotion, and memory are a few of the many things governed by the brain. Together, the brain and spinal cord that extends from it make up the central nervous system. The central nervous system is made of nerve cells called neurons, which are connected to each other via axons and dendrites. The neurons send electrochemical signals with the axons and receives these signals through the dendrites, forming the basis of the brain's complex functions. These nerve cells require fuel to be able to function. The brain consumes about 20% of the energy used in the entire body [6]. The supply of fuels like glucose or ketone bodies to the brain as well as the disposal of the waste products is regulated by a system of fluids. The flow of these fluids is quite complex and especially the drainage of these waste products is an ongoing topic of research [7][8]. Among other things the drainage of these waste products is a function of the cerebrospinal fluid (CSF) in the brain.

CSF is a clear, colourless watery fluid found in the brain and spinal cord of the human body. Within the brain CSF is contained in the brain ventricles and the cranial subarachnoid spaces and within the spine it is found in the spinal subarachnoid spaces [9]. These subarachnoid spaces are a space between two membranous layers enveloping the brain and the spinal cord [10]. CSF has various functions within the brain as it provides protection, assists nourishment, and provides a way of waste removal.

As the brain is floating in CSF it allows the brain to become buoyant, reducing the effective weight of the brain from its normal 1500 grams to only 50 grams [11]. This reduction in weight lessens the forces applied to the brain parenchyma and cerebral vessels during mechanical injury, such that it serves as a shock absorber for the brain when the cranium is hit. Furthermore the CSF functions as a way to protect the brain from pressure fluctuations. The skull is a rigid structure with a fixed volume containing three components: brain tissue,

intracranial vascular volume and intracranial CSF. Only the CSF and blood can be displaced to maintain a constant intracranial volume and pressure without causing any damage [12]. The major conduit of nutrient supply to the brain is through the CSF. Substrates needed by the brain are transported from the blood, through the choroid plexus, into the CSF, and then diffuse into the subarachnoid spaces for transportation to their sites of action within the brain [11]. As the CSF flows from the third ventricle throughout the brain it is also a transporter for hormone releasing factors, opioids and other neuroactive substances [12]. Thirdly and last CSF has a role in the excretion of the potentially toxic by-products of cerebral metabolism. As the brain lacks a lymphatic system, substances such as proteins, including amyloid- $\beta$  which can be affiliated with several disorders like Alzheimer's [13], leaving the brain's tissue have to do so through the perivascular spaces or by direct diffusion into the subarachnoid spaces where it flows with the CSF to eventually be absorbed by the arachnoidal villi into the cerebral veins [14]. This function is part of the glymphatic system, which is a macroscopic waste clearance system of soluble proteins and metabolites from the central nervous system [15].

Given the crucial role of CSF within the brain and in the clearance of waste products from the brain it is important to have a global understanding of the production and flow of CSF throughout the brain. In figure 2.1 a schematic display of the ventricular system is shown. This is a system of four ventricles, two lateral ventricles, the third ventricle and the fourth ventricle, which are connected by several channels. Cerebrospinal fluid is produced by a specialised tissue called the choroid plexus. These choroid plexuses are located in the walls of the lateral ventricles and in the roofs of the third and fourth ventricles. A total of around 150 to 250 ml of CSF is present in the body at any one time [16]. About a sixth of the CSF is located in the ventricles, the rest is present in the subarachnoid spaces [11]. CSF is being produced continuously resulting in a circulation of the fluid around the central nervous system. With around 500 ml of CSF being produced daily the fluid is renewed multiple times a day. The pathway of the CSF is as follows:

1. The CSF passes from the lateral ventricles to the third ventricle through the interventricular foramen
2. From the third ventricle, the CSF flows through the cerebral aqueduct to the fourth ventricle
3. From the fourth ventricle, some CSF flows through a narrow passage and enters the central canal. However, the majority of CSF passes through another opening into the cisterna magnum.
4. From there, the CSF flows through the subarachnoid space of the brain and the spinal cord.
5. Finally, the CSF is reabsorbed through arachnoid granulations.

The characteristics and properties of CSF are identical to those of water. Research has been done on the viscosity properties of CSF as it was questioned whether the high protein content would change the viscosity and the newtonian fluid behaviour, however no significant changes were observed [18]. Furthermore did the measurements result in a viscosity value in the range of 0.7 - 1 mPa.s at 37 °C, which is in accordance with the properties of water and thus confirming the watery fluid properties.

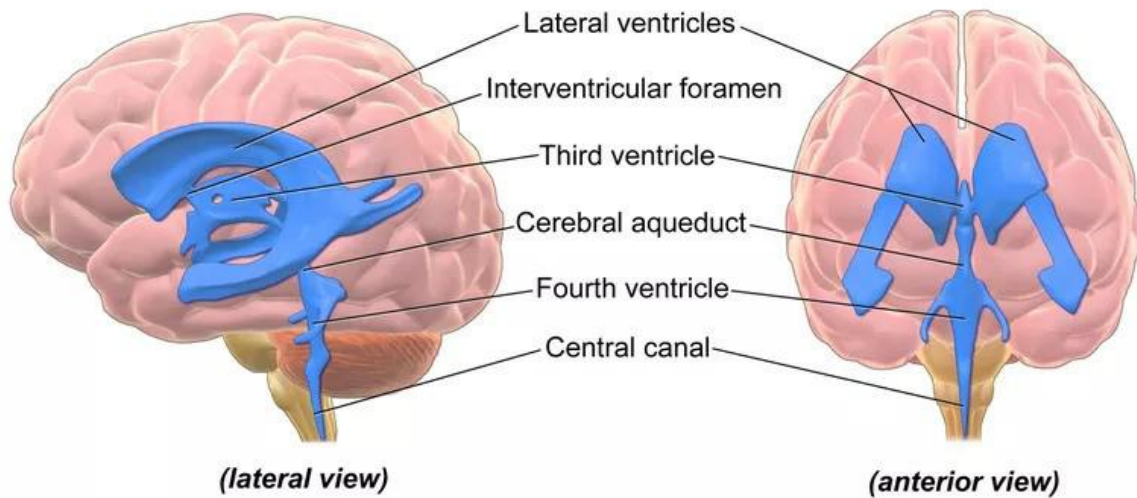


Figure 2.1: Schematic display of the ventricular system [17]

## 2.2 Pial arteries and perivascular spaces

As mentioned in the previous section CSF flows through the subarachnoid spaces of the brain where it functions as a sink for brain extracellular solutes, but it was not yet explained how solutes from the brain move from the parenchyma to the CSF. Recent research using tracer particles have shown that CSF enters the brain parenchyma along perivascular spaces that surround penetrating arteries [19][20]. This thesis is focused on the flow of CSF in those perivascular spaces.

Perivascular spaces (PVS) of the brain, often called Virchow-Robin spaces, are generally considered to be expansions containing fluid around small vessels. In general PVS include a variety of passageways around arterioles, capillaries and venules in the brain, along which a range of substances can move [21]. Although perivascular spaces were first identified over 150 years ago, they have come to prominence recently owing to advances in knowledge of their role in the brain waste clearance systems [22]. PVS can be visualised *in vivo* using MRI, where they appear as structures following the course of the blood vessels penetrating the cerebral parenchyma. In figure 2.2 two PVS are shown, one surrounding a pial artery and one surrounding a penetrating artery.

Pial arteries are the larger arteries within the brain, they lie on the surface of the brain [23]. The pial arteries branch into penetrating arteries and parenchymal arterioles that lie within and supply the brain parenchyma. Pial arteries serve a vital function within the brain and the regulation of cerebral blood flow [24]. When there is an increased metabolic demand by the cerebral cortex, caused by, for example, increased activity, the largest arteries known as the internal carotids and vertebrals remain unaltered. However the pial arteries dilate in order to remain a constant arterial pressure [25]. Pial arteries are round shaped and have

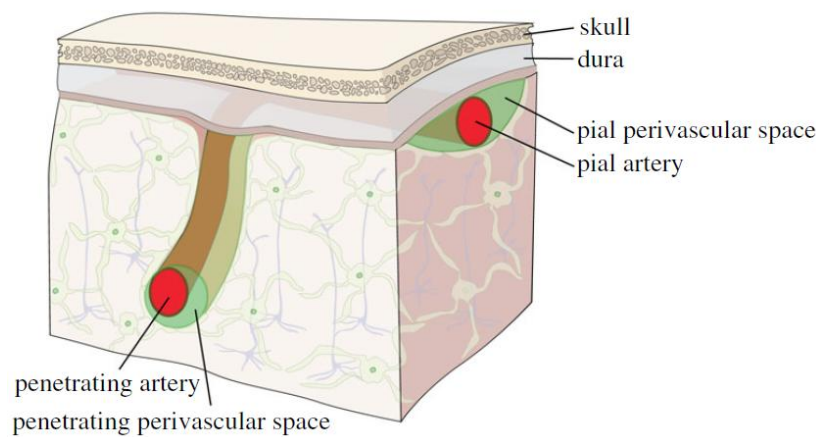


Figure 2.2: Schematic diagram of the PVS around a pial artery and a penetrating artery in the brain [5]

a diameter between 200 and 1200 micrometer, a general classification can be made between small ( 200 micrometer), medium ( 600 micrometer) and large ( 1000 micrometer) sized arteries [26]. Recent measurements of periarterial flows in the mouse brain have shown that the size of PVS around pial arteries is comparable to the diameter of the artery itself [27], this is in accordance with in vivo experiments using fluorescent dyes [28].

As these PVS surround the arteries it was long assumed to be shaped as a circular annulus, however recent research shows that the profile is flattened, often two-lobed and sometimes eccentric [5]. As such it offers less viscous resistance to the flow. Figure 2.3 shows an image of a cross-section of the brain where a blood vessel and corresponding PVS is easily identified. However different images of arteries with corresponding perivascular spaces show slightly differing shapes [28][5]. In general however the shape of the perivascular spaces around a pial artery forms an annular region, elongated in the direction along the skull which is also clearly identifiable in figure 2.3.

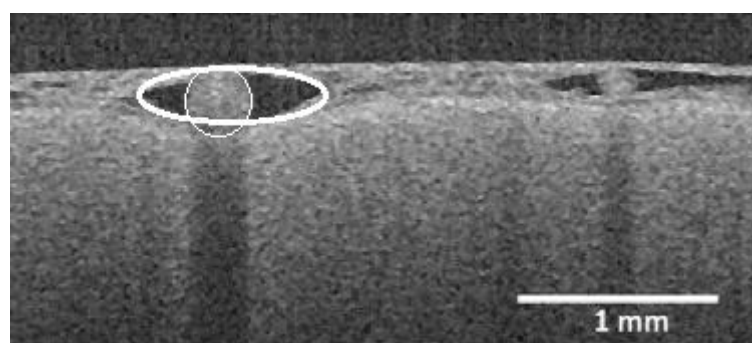


Figure 2.3: Perivascular space around a human artery [29] with a circular fit around the blood vessel, thin line, and an elliptical fit around the perivascular space, thick line.

### 2.3 Cerebrospinal fluid flow in perivascular spaces

The flow behaviour of CSF in PVS is a topic of ongoing research [27][30][31][32][33]. Measurements of CSF fluid are not possible in humans, due to ethical reasons, therefore the only measured in vivo data is from rodent brains. The brains of rodents and humans are however remarkable relatable [34][35], which allows the results of these measurements to be applicable and scaled to the human brain.

Currently the best and most used method to measure the CSF flow in vivo is by particle tracking. In this method fluorescent polystyrene microspheres of about 1 micrometer in diameter are injected into the cisterna magnum by a needle. Using a microscope, a high speed camera and a power LED images are at 30 Hz. The recording of the images is done through a cranial window a bit further down the PVS, such that static and stuck microspheres are eliminated. With the help of an imaging software the vessels with microspheres in the PVS were then analysed and tracked to obtain results on the flow speed [29][27]. The results of both research groups are in accordance with each other, concluding that CSF flow in PVSs has two components, a constant bulk flow in the direction of the blood flow with an average velocity of approximately  $20 \mu\text{m/s}$ , and an oscillatory flow in phase with the heartbeat induced arterial pulsations with a peak velocity of  $10 \mu\text{m/s}$ .

These microsphere particle tracking measurements are widely accepted, however there have been studies suggesting that the observed bulk flow in these measurements is driven by the injection of the microspheres into the cisterna magnum [31]. To be able to eliminate this variable improved measurements have been performed using a double syringe method. In this system two syringes are inserted into the cisterna magnum, where one injects fluid with tracer particles while the other simultaneously withdraws an equal amount of fluid. The researchers performed measurements using the single syringe method and the dual syringe method as shown in figure 2.4.

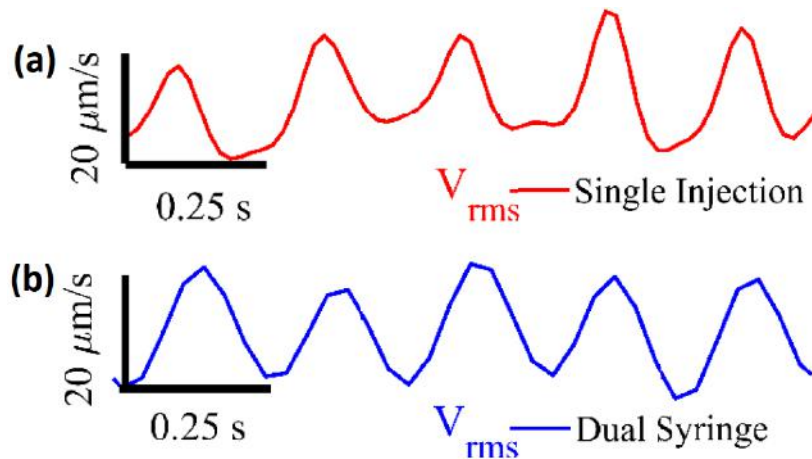


Figure 2.4: CSF flow measurements done by single (a) and dual (b) syringe methods [31]

As can be seen the variation between the two injection protocols does not exceed animal-to-animal variation, therefore it can be concluded that the results obtained by the single injection protocols are valid. The researchers also measured the heartbeat and respiration of the mice simultaneously with the particle tracking measurements. A delay of about 0.05s is seen between peaks in the root mean square velocity of the particle tracking measurements and the results of the electrocardiogram, therefore it is concluded that the CSF flow in PVS

is strongly modulated by the cardiac cycle. No such correlation is found with the respiration cycle [31]. Next to these measurement the flow shape was determined to be consistent with laminar, viscous-dominated flow. The parabolic-like velocity profile is the fastest in the centre of the PVS with velocities reaching up to  $50 \mu\text{m/s}$  and zero at the wall. The typical progression of a microsphere in the PVS is shown in figure 2.5 over 2 seconds of measurement time.

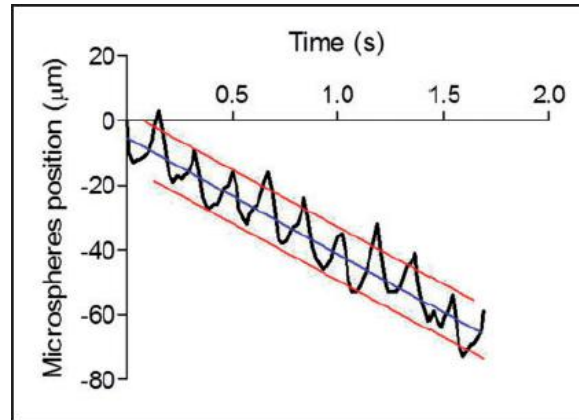


Figure 2.5: Oscillating microspheres in the PVS of a mice [29]

## Chapter 3

# Lattice Boltzmann theory

The lattice Boltzmann Method (LBM) is a powerful simulation technique for single and multi-phase flows in relatively complex geometries. The LBM has its origin in the late 1980s with the Lattice Gas Methods, however the specific development of the LBM started only about 20 years ago. The popularity of the method is rapidly rising due to several advantages the method has compared to the more traditional Computational Fluid Dynamics (CFD) methods. One of those advantages is the fact that the LBM is able to easily run on parallel processing cores, which makes the method very suitable for use with super computers. Unlike conventional continuous-field Navier-Stokes solvers, the LBM doesn't solve for the Navier-Stokes equations, but describes the fluid as moving particle distributions from which it solves the macroscopic quantities such as density and pressure. In figure 3.1 several approaches to CFD are shown, where they are ranked based on their preferred application range of system size and system complexity. It can be seen that the LBM resides somewhere between the continuum solver of the Navier-Stokes equations and the molecular approach and is a good choice for a broad range of system sizes with relatively complex geometries.

The Navier-Stokes Dynamics shown in the bottom left of figure 3.1 are a continuum solver. A blob of fluid is considered to be continuum, where the individual particle dynamics are not considered. Using the conservation laws on an infinitesimal small control volume sets of ordinary differential equations or partial differential equations can be obtained. The Navier-Stokes equations are a famous example of this approach. As such the fluid flow problem is solved on a macroscopic scale, however due to the neglecting of individual particle dynamics this could pose a problem in situations where inter molecular interactions play a significant role.

The Molecular Dynamics shown in the top right of figure 3.1 solve the fluid problem from the bottom up, thus starting at the separate particles. For each particle, the location and directional velocity is considered and the system is solved by applying momentum conservation for the collisions between other molecules and the boundaries. Macroscopic properties like density and pressure are however not explicitly stated, but can be derived from the kinetic energy of the particles. These methods are very accurate and useful in complex geometries, however the limitation is in the system size as these problems can become extremely computational heavy.

Now this is where the LBM comes into play. The method is able to solve the problem at a macroscopic scale, yet still has the advantages of including particle interactions. With the use of statistical mechanics Ludwig Boltzmann derived the Boltzmann transport equa-

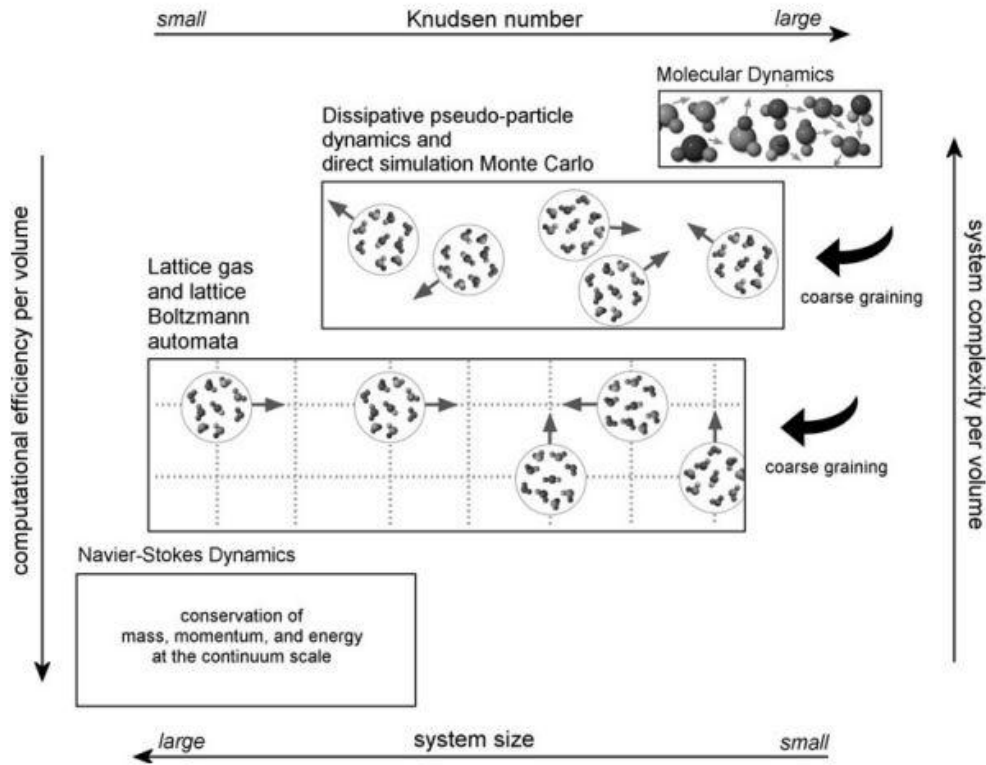


Figure 3.1: Approaches to computational fluid dynamics together with their preferred range of applicability [36]

tion which is the foundation for the LBM. In this chapter the framework of the LBM will be presented with the required derivations and assumptions. First in chapter 3.1 the derivation of the Boltzmann equation is given. Then the equation is improved by deriving a solution for the collision term in section 3.2. After this the improved discretized version will be derived in section 3.3. In section 3.4 the implementation of boundary conditions in the LBM is explained such that a solution can be obtained. Finally in section 3.5 the conversion between physical units and lattice units is described and the selection of several parameters and their constraints are explained.

### 3.1 The Boltzmann equation

The basic concept of the the Lattice Boltzmann method is, as mentioned earlier, that it is possible to describe interacting particles that are not in equilibrium by a statistical expression that takes a huge number of these particles into account. The method is thus not able to describe the behaviour of single particles as it does not consider the position and momentum of a single particle, but it considers the chance that a certain particle has a certain position and a certain momentum which is described by the probability density function. Even though the method uses simple mechanical laws, it is proven that the Boltzmann equation can accurately describe fluid flows [37].

The Boltzmann equations describes the system by a distribution function that resides in a so called *phase space*, which is a space in which the coordinates are given by the the position and momentum vectors at a certain time. As such the phase space is six dimensional, containing three position components and three momentum components. Resulting in a

description of the probability distribution function as follows:

$$f(\mathbf{x}, \mathbf{p}, t) \quad (3.1)$$

This is called a single particle distribution function as it does not contain any information about the other particles. To elaborate on this the probability density function can be given for the probable number of molecules with position coordinates in the range of  $x \pm dx$  and momentum coordinates  $p \pm dp$  as follows:

$$f(\mathbf{x}, \mathbf{p}, t)d^3x d^3p \equiv f(\mathbf{x}, \mathbf{p}, t)d\mathbf{x}d\mathbf{p} \quad (3.2)$$

An external force  $\mathbf{F}$  that is small relative to intermolecular forces is introduced to induce movement. If there are no collisions between particles, then at time  $t+dt$ , the new positions of molecules starting at  $\mathbf{x}$  are:

$$\mathbf{x} + \left(\frac{\mathbf{p}}{m}\right) dt = \mathbf{x} + \left(\frac{d\mathbf{x}}{dt}\right) dt = \mathbf{x} + d\mathbf{x} \quad (3.3)$$

And the new momenta are:

$$\mathbf{p} + Fdt = \mathbf{p} + \frac{d\mathbf{p}}{dt} dt = \mathbf{p} + d\mathbf{p} \quad (3.4)$$

Thus, when the positions and momenta at a certain time  $t$  are known, the particle distribution function at a future time  $t + dt$  follows from:

$$f(\mathbf{x} + d\mathbf{x}, \mathbf{p} + d\mathbf{p}, t + dt)d\mathbf{x}d\mathbf{p} = f(\mathbf{x}, \mathbf{p}, t)d\mathbf{x}d\mathbf{p} \quad (3.5)$$

This is known within the Lattice Boltzmann method as the streaming process. It should however be noted that, due to the large number of particles, moving through the space without collisions is an unrealistic assumptions. Therefore, collisions should be taken into account. These collisions result in two problems, either particles starting at  $(\mathbf{x}, \mathbf{p})$  and not arriving at  $(\mathbf{x}+d\mathbf{x}, \mathbf{p}+d\mathbf{p})$  or particles arriving at  $(\mathbf{x}+d\mathbf{x}, \mathbf{p}+d\mathbf{p})$  that did not start at  $(\mathbf{x}, \mathbf{p})$ . To be able to account for these collisions a source term  $\Gamma$  is added to the Boltzmann equation, giving the total expression for the first order distribution over time as:

$$f(\mathbf{x} + d\mathbf{x}, \mathbf{p} + d\mathbf{p}, t + dt)d\mathbf{x}d\mathbf{p} = f(\mathbf{x}, \mathbf{p}, t)d\mathbf{x}d\mathbf{p} + \Gamma d\mathbf{x}d\mathbf{p}dt \quad (3.6)$$

Dividing both sides of the equation by  $d\mathbf{x}d\mathbf{p}$  and performing a first order Taylor series expansion of the left hand side results in the following expression:

$$f(\mathbf{x} + d\mathbf{x}, \mathbf{p} + d\mathbf{p}, t + dt) = f(\mathbf{x}, \mathbf{p}, t) + \frac{\partial f(\mathbf{x}, \mathbf{p}, t)}{\partial \mathbf{x}} d\mathbf{x} + \frac{\partial f(\mathbf{x}, \mathbf{p}, t)}{\partial \mathbf{p}} d\mathbf{p} + \frac{\partial f(\mathbf{x}, \mathbf{p}, t)}{\partial t} dt \quad (3.7)$$

Substitution of equation 3.7 into equation 3.6 (note that both sides of the equation have been divided by  $d\mathbf{x}d\mathbf{p}$ ) results in the following:

$$\frac{\partial f(\mathbf{x}, \mathbf{p}, t)}{\partial \mathbf{x}} d\mathbf{x} + \frac{\partial f(\mathbf{x}, \mathbf{p}, t)}{\partial \mathbf{p}} d\mathbf{p} + \frac{\partial f(\mathbf{x}, \mathbf{p}, t)}{\partial t} dt = \Gamma dt \quad (3.8)$$

Dividing by  $dt$  this gives the Boltzmann equation:

$$\frac{\partial f(\mathbf{x}, \mathbf{p}, t)}{\partial t} + \frac{d\mathbf{x}}{dt} \cdot \frac{\partial f(\mathbf{x}, \mathbf{p}, t)}{\partial \mathbf{x}} + \frac{d\mathbf{p}}{dt} \frac{\partial f(\mathbf{x}, \mathbf{p}, t)}{\partial \mathbf{p}} = \Gamma \quad (3.9)$$

Using Newton's second law it is known that:

$$\frac{d\mathbf{x}}{dt} = \frac{\mathbf{p}}{m} \quad \text{and} \quad \frac{d\mathbf{p}}{dt} = \frac{d\mathbf{c}}{dt} \cdot m = \mathbf{F} \quad (3.10)$$

When combining these expressions with equation 3.9 and leaving out the phase space indication from the particle distribution function for the sake of clarity one obtains:

$$\frac{\partial f}{\partial t} + \frac{\mathbf{p}}{m} \cdot \frac{\partial f}{\partial \mathbf{x}} + \mathbf{F} \cdot \frac{\partial f}{\partial \mathbf{p}} = \Gamma \quad (3.11)$$

The above equation is the generally used expression for the Boltzmann equation with external forces. A simplification used in the remainder of this chapter includes the use of the Boltzmann equation without external forces, as in the discretized version most cells are not subjected to external forces. Equation 3.12 represent the Boltzmann equation without external force, here the velocity vector is substituted in for the  $\frac{\mathbf{p}}{m}$  term and the  $\frac{df}{d\mathbf{x}}$  term is rewritten by using the  $\nabla$ -operator.

$$\frac{\partial f}{\partial t} + \mathbf{c} \cdot \nabla f = \Gamma \quad (3.12)$$

## 3.2 Bhatnagar Gross Krook relaxation

In the Boltzmann equation shown in equation 3.11 it is still unclear how to solve the collision term  $\Gamma$ . Boltzmann's original collision operator is of the form of a complicated and cumbersome double integral over the velocity space, which considers all the possible outcomes of two-particle collisions [38]. However, the collision operators used in the LBM are generally based on the much simpler approach introduced by Bhatnagar, Gross and Krook (BGK) [39]. This method is commonly referred to in literature as the BGK single relaxation method.

The discretized version of the basic form of the Lattice Boltzmann equation as shown in equation 3.6 can be given as:

$$f_i(\mathbf{x} + \mathbf{e}_i \Delta t, t + \Delta t) = f_i(\mathbf{x}, t) + \Omega_{ij} \quad (3.13)$$

In which  $\mathbf{e}_i$  is the discretized velocity vector and the operator  $\Omega$  is the collision term. As such the first two terms represent the streaming process and the last term represents the collision process. In the BGK relaxation method the collision function is replaced with a term that suffices for single phase flows:

$$\Omega = \frac{1}{\tau} (f^{eq} - f) = \omega (f^{eq} - f) \quad (3.14)$$

This operator can be interpreted as the tendency of the population to approach its equilibrium state after a certain time  $\tau$ . As such this process is also called "relaxation towards equilibrium", where  $\tau$  is called the relaxation time and  $\omega$  the collision frequency. The BGK operator also makes sense logically, as a larger difference between the current distribution and the equilibrium distribution will result in a larger term and thus more collisions will occur in order to reach equilibrium. The collision frequency  $\omega$  in the BGK operator can be seen as a form of artificial viscosity, which will be explained later on in section 3.5.

Substituting the BGK operator into the collision term of equation 3.12 results in the following term for the LBM equation using the BGK operator [40].

$$\frac{\partial f}{\partial t} + \mathbf{c} \cdot \nabla f = \omega (f^{eq} - f) \quad (3.15)$$

In which a clear distinction can be seen between the left hand side, the streaming part, and the right hand side, the collision part. To be able to use the BGK operator the equilibrium distribution function needs to be defined first. This distribution is known to be equal to the Maxwell distribution as shown in equation 3.16, which describes the possibility of a particle being in a certain velocity state. In the Maxwell-Boltzmann distribution the term  $4\pi c^2$  in front of the equation is the result of the evaluation of the particle distribution with certain speed  $c = \sqrt{c_x^2 + c_y^2 + c_z^2}$ , which in the phase space results in all particles on the surface area of a sphere.

$$f^{eq}(c) = 4\pi c^2 \left( \frac{m}{2\pi k_B T} \right)^{3/2} e^{-\frac{mc^2}{2k_B T}} \quad (3.16)$$

In this equation,  $m$  is the mass of the molecule in  $[kg]$ ,  $T$  is the temperature of the system in  $[K]$  and  $c$  is the particle velocity in  $[m/s]$ . In the LBM BGK model a slightly different version of the Maxwell-Boltzmann distribution, where the individual components of the velocity are taken into account, is used. As a result of this change the velocity vector is used instead of a scalar and the spherical area in the phase space is eliminated such that equation 3.16 becomes [41]:

$$f(\mathbf{c}) = \left( \frac{m}{2\pi k_B T} \right)^{3/2} e^{-\frac{m\mathbf{c}^2}{2k_B T}} \quad (3.17)$$

Note that  $\mathbf{c}$  is now a vector of the different velocity components. Equation 3.17 is now multiplied by the macroscopic density  $\rho$  in order to scale the normalised distribution and make it specific for the system. Furthermore a gas will be considered which has a non-zero macroscopic velocity such that the equation changes to:

$$f^{eq} = \frac{\rho}{(2\pi R_{sp} T)^{3/2}} \exp\left(-\frac{(\mathbf{c} - \mathbf{u})^2}{2R_{sp} T}\right) \quad (3.18)$$

In which the specific gas constant is introduced as  $R_{sp} = \frac{K_b}{m}$  which has the units of  $[Jkg^{-1}K^{-1}]$ . In order to perform a Taylor series expansion the exponential term is rewritten to eliminate the quadratic term:

$$f^{eq} = \frac{\rho}{(2\pi R_{sp} T)^{3/2}} \exp\left(-\frac{\mathbf{c} \cdot \mathbf{c}}{2R_{sp} T}\right) \exp\left(\frac{2(\mathbf{c} \cdot \mathbf{u}) - \mathbf{u} \cdot \mathbf{u}}{2R_{sp} T}\right) \quad (3.19)$$

The second term in the equation is now approximated with a Taylor series that is truncated at the second order:

$$f^{eq} = \frac{\rho}{(2\pi R_{sp} T)^{3/2}} \exp\left(-\frac{\mathbf{c} \cdot \mathbf{c}}{2R_{sp} T}\right) \left[ 1 + \frac{2(\mathbf{c} \cdot \mathbf{u}) - \mathbf{u} \cdot \mathbf{u}}{2R_{sp} T} + \frac{(2(\mathbf{c} \cdot \mathbf{u}) - \mathbf{u} \cdot \mathbf{u})^2}{8(R_{sp} T)^2} + \dots \right] \quad (3.20)$$

To get rid of the exponential term in the equation the following substitution is used:

$$W(\mathbf{c}) = \frac{1}{(2\pi R_{sp} T)^{3/2}} \exp\left(-\frac{\mathbf{c} \cdot \mathbf{c}}{2R_{sp} T}\right) \quad (3.21)$$

The equilibrium probability density function that is most commonly used in the BGK LBM method is obtained after some rewriting and eliminating all terms of third or higher order.

$$f^{eq} = \rho W(\mathbf{c}) \left[ 1 + \frac{2(\mathbf{c} \cdot \mathbf{u}) - \mathbf{u} \cdot \mathbf{u}}{2R_{sp} T} + \frac{(\mathbf{c} \cdot \mathbf{u})^2}{2(R_{sp} T)^2} \right] + \mathcal{O}(u^2) \quad (3.22)$$

With the equilibrium distribution function derived the last unknown in the Lattice Boltzmann equation, the collision term, is also known.

### 3.3 Discretization

The Boltzmann equation as shown in equation 3.11 is particularly complicated as its complete form with the collision operator written more explicitly results in a nonlinear integral differential equation [37]. According to Harris [42], 50 years elapsed from the time the equation was derived before an approximate solution was found. Lattice Boltzmann methods vastly simplify the original approach by reducing the number of possible particle spatial positions and microscopic momenta from a continuum to a discretized grid and similarly discretizing time into distinct steps. As such the lattice element is introduced to confine particle positions to the nodes of a lattice.

There are a multitude of varying lattice elements that can be used in the LBM each denoted by  $D_nQ_m$ , with  $n$  giving the dimensions of the lattice and  $m$  giving the number of flow directions. Within this thesis the simulations are performed using a D3Q19 stencil. However in this section the D2Q9 stencil, shown in figure 3.2 is used as an example due to the more simple and clear visualisation.

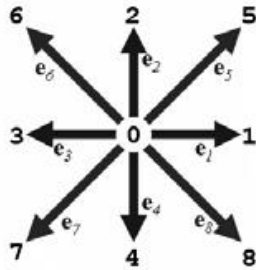


Figure 3.2: D2Q9 Lattice element [37]

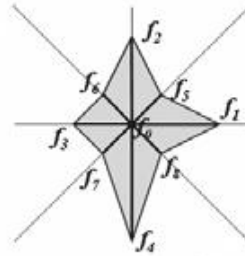


Figure 3.3: D2Q9 distribution function example [37]

As can be seen in figure 3.2 a total of 9 streaming directions are possible, as a particle at rest, index 0, stays on the same node. The different streaming directions are given by the discrete velocity vector  $\mathbf{c}_i$ :

$$\mathbf{c}_i = \begin{cases} (0, 0) & i = 0 \\ (1, 0), (0, 1), (-1, 0), (0, -1) & i = 1, 2, 3, 4 \\ (1, 1), (-1, 1), (-1, -1), (1, -1) & i = 5, 6, 7, 8 \end{cases} \quad (3.23)$$

The distribution function can conveniently be seen as a typical histogram representing a frequency of occurrence, an example of such a distribution is shown in figure 3.3. For each streaming direction a weight factor  $w_i$  is introduced, which is dependent on the lattice element used. The weight factors for a D2Q9 element are as follows:

$$w_i = \begin{cases} 4/9 & i = 0 \\ 1/9 & i = 1, 2, 3, 4 \\ 1/36 & i = 5, 6, 7, 8 \end{cases} \quad (3.24)$$

Using these lattice elements the discrete version of the Boltzmann Transport equation that can be used along these specific directions is as follows:

$$\frac{\partial f_i}{\partial t} + \mathbf{c}_i \cdot \nabla f_i = \omega (f_i^{eq} - f_i) \quad (3.25)$$

In this discrete form of the Boltzmann Transport equation the discretized version of the equilibrium distribution function is used. This discrete function can be derived from equation 3.22 using the substitution below:

$$c_s^2 = R_{sp}T \quad (3.26)$$

In which  $c_s$  is the lattice speed of sound, which depends on the chosen lattice element. As a result the following discrete equilibrium function is obtained:

$$f_i^{eq} = \rho w_i \left[ 1 + \frac{2(\mathbf{c}_i \cdot \mathbf{u}) - \mathbf{u} \cdot \mathbf{u}}{2c_s^2} + \frac{(\mathbf{c}_i \cdot \mathbf{u})^2}{2c_s^4} \right] + \mathcal{O}(u^2) \quad (3.27)$$

In which  $w_i$  are the weight factors corresponding to those shown in equation 3.24. Furthermore for both D2Q9 and D3Q19 lattice elements the speed of sound is given by  $c_s^2 = 1/3$ , which simplifies the equation as follows:

$$f_i^{eq} = \rho w_i \left[ 1 + 3(\mathbf{c}_i \cdot \mathbf{u}) - \frac{3}{2}(\mathbf{u} \cdot \mathbf{u}) + \frac{9}{2}(\mathbf{c}_i \cdot \mathbf{u})^2 \right] + \mathcal{O}(u^2) \quad (3.28)$$

The conversion of the microscopic velocities and particle density functions to the macroscopic variables of the fluid is rather straightforward. The distribution function as shown in figure 3.3 can be seen as direction-specific fluid densities. As such the macroscopic density can be determined as follows:

$$\rho = \sum_{a=0}^8 f_a \quad (3.29)$$

Furthermore the macroscopic velocity  $\mathbf{u}$  is an average of the microscopic velocities  $\mathbf{e}_a$  weighted by the directional densities  $f_a$ :

$$\mathbf{u} = \frac{1}{\rho} \sum_{a=0}^8 f_a \mathbf{e}_a \quad (3.30)$$

These equations allow for a direct transfer from the discrete microscopic velocities and particle density functions to the macroscopic densities and velocities. As such the discrete LBM method can be transferred to a continuum domain representing the fluid's motion.

## 3.4 Boundary conditions

In the previous chapter the framework for a solver for fluid problems is described. However no particular solutions to these flows can be calculated as they are just arbitrary problems. In order to calculate meaningful results boundary conditions and initial conditions are required. Even though relatively speaking the boundary nodes apply to only a small portion of the fluid domain, their influence will be noticed everywhere in the flow solution. In the LBM the boundary nodes are described as the sites with at least one link to a solid and one to a fluid node, this assignment of lattice site types is graphically shown in figure 3.4. In this section the two relevant boundary conditions for this thesis will be explained, which are the bounce-back boundary condition and the Dirichlet boundary condition.

### 3.4.1 Bounce-back boundary condition

The most commonly used boundary condition is the bounce-back boundary condition. This boundary condition is used as the no-slip velocity boundary condition at the fluid-solid interface and is thus used to model walls within the LBM. The basic working principle of the

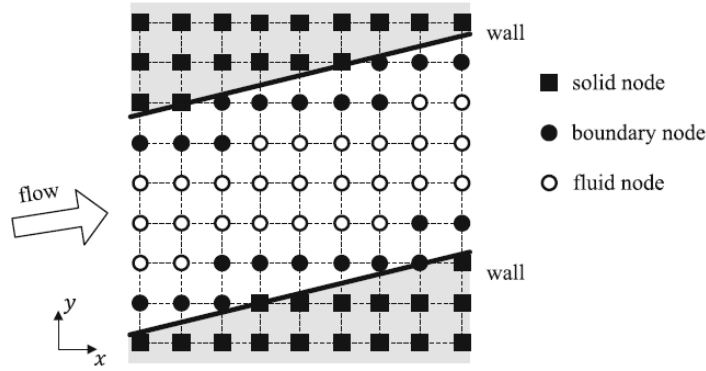


Figure 3.4: Fluid, solid and boundary nodes in an inclined channel[38]

bounce-back boundary condition is that populations hitting a rigid wall during propagation are reflected back to where they originally came from. It may seem counter intuitive that the particles are reflected back rather than bounced forward (i.e. specularly reflected), however one must understand that this implies no relative transverse motion between the fluid and the boundary and thus a no-slip condition on the wall.

An important aspect of the bounce-back boundary condition is the definition of the boundary. There is the fullway bounce-back and the halfway bounce-back method, this is graphically shown in figure 3.5. Within the figure the direction of the arrow represents the particle's direction whereas the grey area is the solid region and the dashed line corresponds to the boundary. It can be seen that the difference between the two methods is the use of the boundary nodes as a storage location. In case of the fullway bounce-back method, (a) in the figure, the particles travel the entire path from the fluid node to the boundary node, where the particle velocity is inverted in the next collision step, after which the fluid is propagated back into the fluid domain at the next time step. When using the halfway method, (b) in the figure, the redirection of the flow is done halfway the time step before the flow reaches the next solid node such that this all takes place during the streaming step.

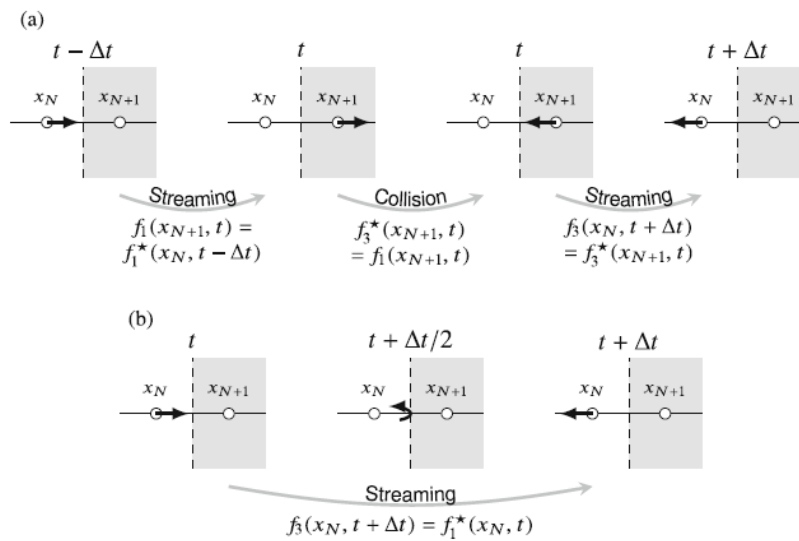


Figure 3.5: Time evolution for a (a) fullway bounce-back and (b) halfway bounce-back boundary condition [38]

It should be noted that despite the naming of the methods both approaches assume that the boundary is located midway between the solid and boundary nodes, as can be seen by the dashed line in figure 3.5. This way the boundary condition is formally second-order accurate, whereas having the bounce-back boundary placed on a lattice node introduces a first-order error. As such both strategies shown in figure 3.5 achieve second-accuracy. If simplicity is the main concern the fullway bounce-back is the preferred choice as the only check that needs to be done is whether a solid node is reached or not, whereas for the halfway scheme each propagation direction needs to be tracked. Yet halfway bounce-back is more accurate for unsteady flows due to the fact that less time steps are required and thus no degradation of the time accuracy of the solution will happen. Furthermore the halfway bounce-back can be implemented without solid nodes.

The implementation of the bounce-back boundary condition into a LBM scheme is done according to equation 3.31. In which the populations leaving the boundary node  $x_b$  at time  $t$  meet the wall surface at time  $t + \frac{\Delta t}{2}$ , where they are reflected back with a velocity  $c_i^- = -c_i$ . The notation of  $f^*$  is used to denote the pre-stream values.

$$f_i^-(x_b, t + \Delta t) = f_i^*(x_b, t) \quad (3.31)$$

### 3.4.2 Dirichlet boundary condition

It can be concluded that the bounce-back boundary condition is a very suitable solution for the walls in a LBM model and even though it can be used at inflow and outflow locations there are other more useful methods for it [43]. Dirichlet boundary conditions allow a macroscopic value, like a velocity or pressure, to be assigned to a point, line or plane. For example a velocity vector is specified at a boundary line:

$$\mathbf{u}_0 = \begin{bmatrix} u_0 \\ v_0 \end{bmatrix} \quad (3.32)$$

Consider a D2Q9 grid shown in figure 3.2 which is placed at a top wall/inlet where an inlet velocity is prescribed according to equation 3.32. After the streaming step there are three unknown directional densities at this lattice node pointing from the boundary into the fluid domain. Together with the unknown density  $\rho$  this means there are four unknowns, which requires 4 equations to solve.

The macroscopic density for this lattice element results in the first equation:

$$\rho = \sum_i f_i = \underbrace{f_0 + f_1 + f_2 + f_3 + f_5 + f_6}_{\text{known}} + \underbrace{f_4 + f_7 + f_8}_{\text{unknown}} \quad (3.33)$$

The momentum equations in both  $x$  and  $y$  directions results in the second and third equation:

$$\rho \mathbf{u} = \sum_i \mathbf{u} f_i = \underbrace{\mathbf{u} (f_2 + f_5 + f_6)}_{\text{known}} - \underbrace{\mathbf{u} (f_4 + f_7 + f_8)}_{\text{unknown}} \quad (3.34)$$

The fourth equation is obtained by assuming that the bounce-back or symmetry condition holds in the direction normal to the boundary [44].

$$f_2 - f_2^{eq} = f_4 - f_4^{eq} \quad (3.35)$$

After some algebraic operations using the known equilibrium distribution functions the unknowns can be solved to implement the boundary condition. The same method applies for a given pressure at the boundary, where the following equation of state can be used:

$$p = c_s^2 \cdot \rho \quad (3.36)$$

### 3.5 Selection of lattice parameters

As the LBM simulations have to represent a physical problem the parameters on the lattice have to be scaled accordingly. As with all fluid problems the non dimensional-parameters that are of influence have to be matched in the physical world and on the lattice. In this thesis the Reynolds numbers is of importance due to the highly viscous laminar flow present in the simulations.

The density distribution function  $f_i$  and the relaxation parameter  $\tau$  are already non dimensional and therefore do not require a conversion. The first step to implement the real world system in the LBM simulation is the selection of the lattice velocity  $C$ . The lattice velocity is often set to be equal to 1 lattice unit per second, such that particles always move to one neighbouring node in one time step.

$$C \equiv \frac{h}{\Delta t} \equiv \frac{\Delta x}{\Delta t} \quad (3.37)$$

In which  $\Delta x$  and  $\Delta t$  are respectively the grid spacing in meters and the time step in seconds. Using the lattice velocity the conversion between physical fluid velocity and lattice fluid velocity is quite straightforward:

$$v_{\text{lat}} = v_{\text{phy}} \frac{\Delta t}{\Delta x} = \frac{v_{\text{phy}}}{C} \quad (3.38)$$

The density, the kinematic viscosity and the dynamic viscosity are coupled directly, such that only two of these have to be given for a fully defined system.

$$\nu = \frac{\mu}{\rho} \quad (3.39)$$

In the LBM an equation of state exists which relates the pressure and the density to each other using the speed of sound on the lattice:

$$P = c_s^2 \rho \quad (3.40)$$

In which the lattice speed of sound can be related to the lattice velocity as shown in equation 3.41. This expression however is not universal for all lattice models but is valid for the commonly used D2Q9 and D3Q19 models. Taking into account that the lattice velocity is chosen to be equal to unity the lattice speed of sound can be defined as follows:

$$c_s = \frac{C}{\sqrt{3}} \equiv \frac{1}{\sqrt{3}} \quad (3.41)$$

As mentioned before viscosity on a molecular scale doesn't really exist, however in the LBM the kinematic viscosity is related to the relaxation frequency, the spatial step and the time step as shown in equation 3.42. This relation also ensures that the LBM simulations follow the macroscopic physics described by the Navier-Stokes equation [38].

$$\nu = \frac{(\tau - \frac{1}{2})}{3} \frac{\Delta x^2}{\Delta t} = \frac{\frac{1}{\omega} - \frac{1}{2}}{3} \frac{\Delta x^2}{\Delta t} \quad (3.42)$$

In this equation the parameter  $\omega$  can be tweaked, which affects the implicitly defined time step. If a larger value of  $\omega$  is chosen, the time step becomes smaller and thus the amount of iterations to achieve the total simulation time increases. In general the value of  $\omega$  has to be lower than 2, but higher than 0.5 to achieve a physical flow. Note that changing the value of  $\omega$  affects the apparent viscosity, however the physical viscosity does not change. The lattice viscosity is defined as follows:

$$\nu_{\text{lat}} = \nu \frac{\Delta t}{\Delta x^2} = \frac{\frac{1}{\omega} - \frac{1}{2}}{3} \quad (3.43)$$

# Chapter 4

## Simulation environment

In this chapter the simulation environment will be explained. This is basically the conversion from the LBM theory to a working simulation model. The used software in this thesis is called APES (Adaptable Poly-Engineering Simulator), which is a bundle of tools for flow simulations. First the APES suite will be explained, after which the individual components of *Seeder* and *Musubi* are discussed and last but not least the software used in the post-processing is mentioned.

### 4.1 APES software

The central environment of the simulations is called the Adaptable Poly-Engineering simulator (APES). An overview of the various modules available within APES is shown in figure 4.1. In this thesis the *Seeder* module is used to generate the mesh after which the *Musubi* module is used to perform the Lattice Boltzmann simulation on this mesh. The *Harvester* module can be used to visualise the mesh prior to running fluid simulations. As has been stated in section 3 the downside of the LBM method is the size of the problem and thus the high computational effort, APES suite is developed for use on parallel computers and with a high parallel efficiency [45][46]. Still a high computer power is required to perform the simulations, this is solved by using the dutch supercomputer *Snellius*.

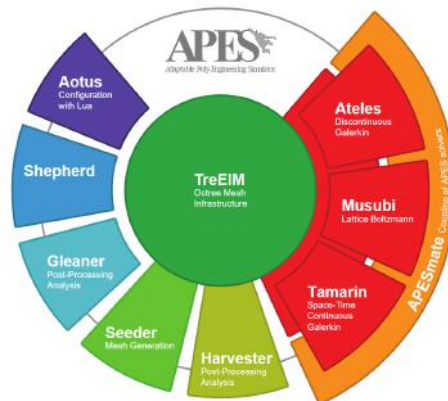


Figure 4.1: Overview of APES components[47]

## 4.2 Seeder

The mesh generation is performed using *Seeder*, which is part of the APES suite as shown in figure 4.1. As mentioned in section 4.1 the simulations are performed using parallelization, therefore a structured grid with equally sized elements is created. The input for *Seeder* is an input file in which the information of the geometry is described. This input file should contain the boundaries of the model, the bounding cube, the refinement level, a seed location, and in the case of complex geometries a STL file which can be created with an external program like *SolidWorks*. All these aspects will be explained in more detail in this section.

In the input file first a cubical outline of the mesh has to be described which has to enclose the complete geometry, this is called the bounding cube. The enclosed geometry is specified by the provided STL file. As such *Seeder* is now able to create an octree mesh with the root node being the bounding cube. *Seeder* uses recursive bisection to generate the mesh. With recursive bisection is meant that on the zeroth level the mesh consist of a single cube. When the mesh is refined this cube is split into eight smaller cubes, with side lengths equal to half the size of the previous cube, hence the name octree. This process is being repeated until the desired element size or number of elements is obtained. As such the number of elements can be determined according to the following formula:

$$n_{elements} = 2^{3 \cdot level} \quad (4.1)$$

The level in this equation is related to the desired spatial step size  $dx$  and the length of the boundary cube:

$$Level = \frac{\log(\frac{L}{dx})}{\log(2)} \quad (4.2)$$

In which L is the largest length in any of the spatial dimensions present in the geometry and thus equal to the bounding cube. The resulting level is rounded up to achieve a whole integer, therefore the spatial step size  $dx$  can be slightly smaller than requested. By defining the size of the bounding cube as a function of the desired element size  $dx$  this problem can be prevented.

At this point the *Seeder* module is able to generate the geometry, however the program still needs information to determine what the fluid, boundary and solid nodes are. Therefore a seed has to be placed somewhere inside of the geometry where a fluid node is located. Everything that is between the walls and this seed is then considered to be part of the fluid geometry and the walls are set as boundary nodes. These boundary nodes still need to be divided into separate regions, which is done in the last part of the input file. Labelling the different boundaries allows the user to define different boundary conditions to these regions in the *Musubi* input file.

The *Harvester* module can be used to process the generated mesh and outputs a geometry file. This module allows the user to check the geometry without having to run fluid simulation which helps in preventing errors early on.

### 4.3 Musubi

With the mesh being generated the LBM simulation can be performed. The Lattice Boltzmann solver *Musubi*, which uses the theory presented in section 3, is used in this thesis. Similar to the *Seeder* module an input file is made to communicate with the solver. Within this input file the physical problem is described, the conversion to certain lattice parameters is performed and the simulation parameters such as time control settings and the tracking of data are set. The options offered by this module will be described in this section.

Within the Lattice Boltzmann the distinction between physical parameters and lattice parameters need to be clear as explained in section 3.5. In the input file of the *Musubi* module the macroscopic physical parameters are specified as well as their lattice counterparts. Furthermore the selection is made for the BGK approximation and thus the relaxation frequency  $\omega$  is also given as input. The selection of this value is rather free of choice but it should be greater than 0 and smaller than 2 following equation 3.43. Lower values of  $\omega$  introduce more viscosity in the system, which can be seen as a dampening of the solution as it means that the initial fluctuations are lower but the time till convergence is increased. It is often desired to have a lower apparent viscosity in the system for the faster convergence time, therefore within this thesis a larger value of  $\omega$  is chosen. Furthermore it should be noted that the selection of  $\omega$  directly influences the time step, meaning a higher  $\omega$  implies a smaller time step.

Within the *Musubi* module a choice has to be made regarding the physical model, which can be either compressible or incompressible. The choice between these two is mainly based on the Mach number in the problem. In the simulations performed in this thesis the Mach number stays well below the compressibility limit, as the lattice fluid speed is less than 0.3 times the lattice speed of sound.

### 4.4 Post-processing

To be able to view the produced results of the *Musubi* solver the *ParaView* program is used. *ParaView* is an open-source, multi-platform data analysis and visualisation application. Within the application users can quickly build visualisations to analyse their data using qualitative and quantitative techniques. When additional analysis is required the data is extracted from *Paraview* and imported in to *MatLab*.

## Chapter 5

# Preliminary flow studies

In this chapter a grid convergence study is performed on a simplified geometry case. The main purpose of this study is to determine the correct grid size for further simulations, which means it has to produce valid results while keeping the computational time as low as possible. Also, these simulations allowed some testing to get familiar with the software and the input parameters.

### 5.1 Geometry

This grid study is performed on a simplified straight geometry which are two concentric tubes as shown in figure 5.1. This geometry is chosen, because for a concentric annulus the exact solution can be derived and thus a direct comparison between the analytical and exact solution can be made. The geometry will be sized to a pial artery and PVS in the human brain, which will be the same size as the geometries in chapter 6 will have.

As described in section 2.2 the diameter of pial arteries range from 200 to 1200 micrometer, but the researchers described the most occurring medium sized arteries to have a diameter size of 600 micrometer [26]. The size of the PVS is still a subject of research, however in the case of a concentric PVS shape it is shown that the radius of the PVS is almost equal to the radius of the artery as shown in equation 5.1 [32]. Therefore the geometry in this study has an inner diameter, representing a pial artery, of 0.6 millimetre and an outer diameter, representing a PVS, of 1.2 millimetre.

$$2 \cdot r_{artery} = r_{PVS} \quad (5.1)$$

With the cross-sectional shape determined only the length of the artery is still unknown. A commonly used parameter for determining the length is the aspect ratio as described in equation 5.2.

$$AR = \frac{Length}{D_{hydraulic}} = \frac{Length}{D_{outer} - D_{inner}} \quad (5.2)$$

Aspect ratios ranging from 5 to 12 have been accepted values for a long time, however research showed that values as high as 24 might be beneficial for turbulent flow simulations [48]. Within this thesis only laminar flow is present and thus lower aspects ratio of around 10 are deemed to be sufficient. This length allows for a complete development of the flow profile and is still limiting the size of the computational domain. In the simulations performed in this chapter a length of 6 millimetre is used for the artery.

## 5.2 Analytical solution

Laminar fluid flow through a concentric annulus is a known problem in literature from which the analytical can be solution can be derived quite easily, as will be shown in this section. Consider a steady laminar flow of a Newtonian fluid with constant density, which is located in a long annular region between two coaxial cylinders of radii  $R_0$  and  $R_i$  as shown in figure 5.1.

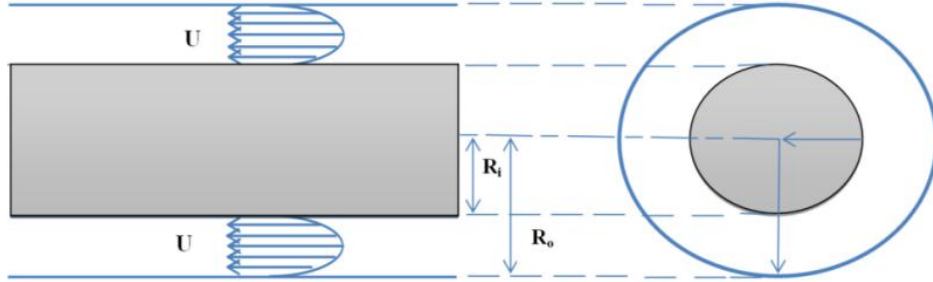


Figure 5.1: Fluid flow between two coaxial cylinders [49]

The governing equation for the exact solution of this described fluid problem is known to be [49]:

$$-\frac{1}{r} \frac{d}{dr} \left( \mu r \frac{dU}{dr} \right) = \frac{P_1 - P_2}{L} = f_o \quad (5.3)$$

In which  $U$  is the velocity along the cylinder,  $\mu$  is the viscosity of the fluid,  $L$  is the length of the region along the cylinders in which the flow is fully developed, and  $P_1$  and  $P_2$  are the pressures at locations  $z = 0$  and  $z = L$ . After some rewriting of equation 5.3 the following formula is obtained:

$$\frac{d}{dr} \left( r \frac{dU}{dr} \right) = \frac{r}{\mu} f_o \quad (5.4)$$

To be able to obtain a solution for the velocity field,  $U(r)$ , equation 5.4 has to be integrated twice with respect to the radius  $r$ . After one integration the following equation is obtained:

$$\frac{dU}{dr} = \frac{1}{\mu} f_o \frac{r}{2} + \frac{C_1}{r} \quad (5.5)$$

And integrating with respect to  $r$  once more results in the following expression for the velocity field:

$$U(r) = \frac{1}{4\mu} f_o r^2 + C_1 \ln r + C_2 \quad (5.6)$$

The only unknowns in this equation are the pressure term,  $f_o$ , which will be solved later on and the two constants,  $C_1$  and  $C_2$ , which will be solved by substitution of the boundary conditions. At both the upper and lower wall of the fluid region a no slip boundary conditions is present, such that the fluid velocity at both ends equals zero. This is mathematically described as follows.

$$r = R_i : U(r) = 0 \quad \text{and} \quad r = R_0 : U(r) = 0 \quad (5.7)$$

Substitution of these boundary conditions results in two equations with two unknowns and can therefore be solved. The results are the following descriptions for the constants:

$$C_1 = \frac{f_o}{4\mu} \frac{R_0^2 - R_i^2}{\ln(R_0/R_i)} \quad \text{and} \quad C_2 = \frac{f_o}{4\mu} R_0^2 - C_1 \ln R_0 \quad (5.8)$$

Substituting the descriptions for the constants back in to equation 5.6 yields the final expression for the velocity profile.

$$U(r) = \frac{f_0 R_0^2}{4\mu} \left[ 1 - \left( \frac{r}{R_0} \right)^2 + \frac{1 - (R_i/R_0)^2}{\ln(R_0/R_i)} \ln \left( \frac{r}{R_0} \right) \right] \quad (5.9)$$

The only remaining unknown in this equation is the pressure term  $f_0$ , which as shown in equation 5.3 is dependent on the pressure drop. An expression for the pressure drop of a laminar fluid flow in a concentric annulus is shown in equation 5.10 [50].

$$\Delta P = \frac{\rho U_z^2}{2} \left( \frac{\lambda L}{2s} \right) \quad (5.10)$$

Where  $\Delta P$  is the pressure difference between the inlet and outlet of the channel,  $\rho$  the fluid density,  $U_z$  the mean axial velocity,  $L$  the channel length and  $s$  the channel height. In this case the channel height is derived from the hydraulic diameter as  $D_H = 2s$ . Therefore the only unknown in equation 5.10 is the friction coefficient  $\lambda$ . The friction coefficient in narrow static annular channels for laminar flow is stated in literature as follows [51]:

$$\lambda_l = \frac{96}{Re_z}, \quad \text{with} \quad Re_z = \frac{2\rho U_z s}{\mu} \quad (5.11)$$

In this equation all parameters are known, therefore the friction coefficient can be solved and substituted back in to equation 5.10 from which the coefficient  $f_0$  can be calculated. Using this information the exact solution as described in equation 5.9 can be solved when the mean axial velocity and geometry and fluid parameters are given.

### 5.3 Simulation results

The analytical solution derived in section 5.2 will be compared to several LBM simulations using different grid sizes. In table 5.1 the geometrical and fluid parameters of the test case are shown. The input velocity used is a constant velocity in order to be able to compare the flow to the analytical solution derived in the previous section. The simulation time is kept as short as possible, while still achieving a fully developed flow, to further reduce the computational time.

Table 5.1: Simulation parameters for preliminary flow studies

Parameter	Value	Unit	Parameter	Value	Unit
Length	6	[mm]	Density	9.933E-7	[kg/mm <sup>3</sup> ]
Inner diameter	0.6	[mm]	Viscosity	6.913E-7	[kg/(mm · s)]
Outer diameter	1.2	[mm]	Velocity	0.2	[mm/s]
Pressure	1	[Pa]	Omega	1.6	[-]

A total of 5 LBM simulations are performed. The descriptions of the simulations are shown in table 5.2. Each consecutive simulation the spatial step size is halved and therefore the amount of elements in vertical direction is doubled. The time step is reduced for finer grid sized due to the definition for the time step as a parameter that is implicitly dependent on the spatial step size.  $N$  is the total number of elements in the domain whereas  $N_{vert}$  is the amount of elements between the outer and inner radii in vertical direction.

Table 5.2: Simulation results of preliminary flow studies

Grid	dx	dt	N	$N_{vert}$
1	0.075	3.37e-04	5356	3
2	0.0375	8.42e-05	53130	7
3	0.01875	2.1e-05	496156	15
4	0.009375	5.26e-06	3918500	31
5	0.0046875	1.32e-06	32085468	63

In figure 5.2 the fluid velocity over time is plotted for the first 0.2 seconds of simulation time for a probe located at position  $[X,Y,Z] = [0.7,1.15,5]$ . This probe locations corresponds with a point somewhere near the end of the channel which is located in the centre of the upper region, however the same results should be obtained for probe locations at other depths in the channel. Next to the simulation results the exact solution is plotted as a horizontal line. It can be seen that the coarsest grid size is not able to reach a converged solution in the first 0.2 seconds, however all finer grid sizes are able to achieve a converged solution. Furthermore it can be seen that for a finer grid size the converged solution approaches the exact solution better and the flow converges faster. This more accurate solution is due to a finer grid size being better able to represent the fluid flow and the faster convergence time is due to the smaller time step.

In figure 5.3 the velocity profile in vertical direction is plotted for all the grid sizes after 2 seconds of simulation time. As can be seen the velocity profile approaches the analytical solution more and more accurate as the grid size is refined. The coarsest two grid sizes show significant differences with the exact solution, however the finer 3 grid sizes all approach the exact solution quite accurately. The small difference between the finest grid and the analytical solution can be explained due to numerical errors.

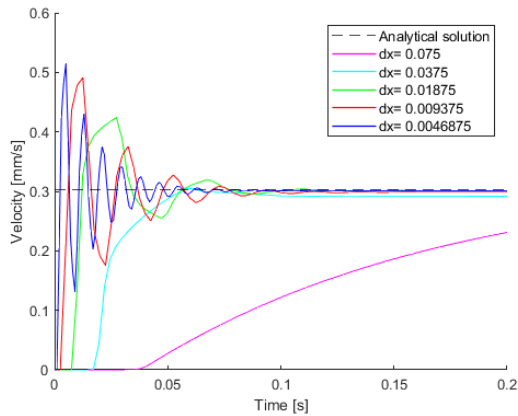


Figure 5.2: Fluid velocity over time for different grid sizes at  $[X,Y,Z] = [0.7,1.15,5]$

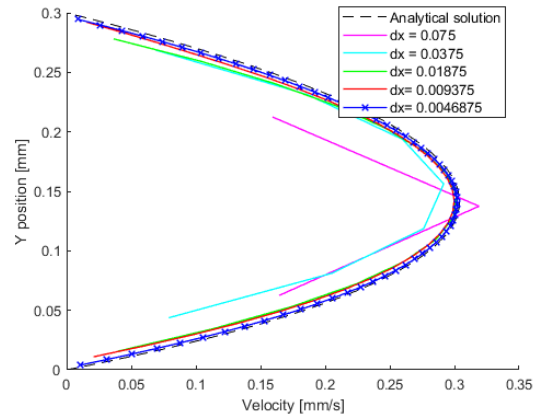


Figure 5.3: Vertical velocity profile for different grid sizes

## 5.4 Convergence

To be able to determine if the results on the finer grid sizes are refined enough a grid convergence study is performed. First of all the classical method is used, in which the error term is plotted on a log-log scale to the mesh size and compared with the assumed discretization error based on the used numerical scheme. The euclidean norm as shown in equation 5.12 will be used for the error term. In which  $N$  is the total number of elements,  $X_h$  is the numerical solution and  $X$  is the analytical solution.

$$L_2(x) = \frac{1}{N} \sqrt{\sum (X_h - X)^2} \quad (5.12)$$

In figure 5.4 the log-log plot of the error terms is shown against the spatial step size. Furthermore the analytical second order accuracy is plotted. It can be seen that the slope of the numerical solutions is slightly less steep than the analytical expectation. This is an expected result. In theory the Lattice Boltzmann method is second order accurate however the use of boundary conditions and grid will reduce this order so that the observed order of accuracy is likely to be lower [52]. However the slope of the finest grid sizes is close enough to assume a converged solution.

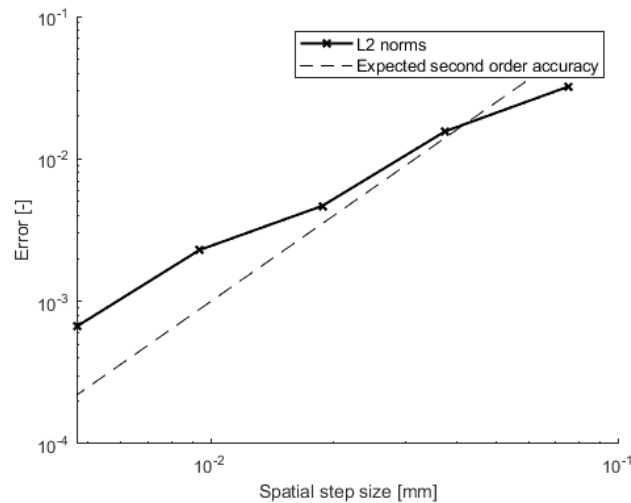


Figure 5.4: L2 norm on different grid sizes

Another way to check for grid conversion is the use of the grid convergence index. In the classical method the observed rate of convergence was determined graphically, however with this method the rate of convergence is quantified. Another advantage to this method is that no analytical solution is required, which is the case in most practical scenario's. To be able to calculate the index three grid sizes are required, therefore only the three finest grid sizes are used here. It should be noted that the derivation and method below is only valid when the refinement ratio  $r$  is a constant, which is the case here as  $r = h_3/h_2 = h_2/h_1 = 2$ . Using the solutions on the different grid sizes the observed order-of-convergence is calculated according to the following formula:

$$p = \frac{\log\left(\frac{f_3 - f_2}{f_2 - f_1}\right)}{\log(r)} \quad (5.13)$$

This results in an observed order of convergence of 1.67, which is in line with figure 5.4 and an order of slightly lower than 2 makes sense as mentioned before.

## Chapter 6

# Straight artery simulations

The first set of simulations that are performed are those of CSF flow simulation in a straight artery's PVS. These simulations build the base of knowledge on which the rest of the simulations shown in later chapters elaborate. The results of these simulations can be interpreted quite well by basic intuition and can therefore easily be checked for mistakes in the code.

The aim of these simulations is to gain insight in the effect of cross-sectional shape changes on the magnitude of the flow and the different cross-sectional velocity profiles resulting from these changes. In these simulations the geometry of the artery and the PVS are heavily simplified, however the CSF parameters and flow behaviour is matched to the real world case. The CSF inlet flow conditions are obtained by scaling the results of measurements done in mice to the human brain size and as such can be considered relatively accurate.

This chapter is divided in several sections, starting with the details about the CSF and the flow of this fluid in the PVS. Then the geometries for these simulations are presented in section 6.2. Finally in section 6.3 the results of the simulations are presented and discussed.

### 6.1 CSF fluid and flow

In section 2.3 a general description of the flow and characteristics of CSF is given, based on measurements and research performed previously. However, most of these measurements are performed on mice and rodents, whereas in these simulations the CSF flow in the human brain is the area of interest. As such several characteristics of the CSF flow such as overall flow speed, oscillation time and oscillation intensity still need to be determined. Furthermore the general characteristics of the fluid are yet to be quantified. Therefore in this section first the the fluid characteristics are quantified, then a quantified description of the CSF flow in mice is given after which the scaling of these flow characteristics to the human brain size is explained.

#### 6.1.1 Cerebrospinal fluid characteristics

To be able to simulate the fluid only two parameters are required, the density and the viscosity, as the remaining parameters required can be derived from these two. As mentioned in section 2.1 CSF behaves like a watery fluid and as such the properties of water are valid to simulate the fluid behaviour. These parameters of water are dependent on the temperature, therefore the temperature within the human body is required, this can safely be assumed

to be on average about 37 °C [53] and thus this temperature is used to determine the CSF properties. The properties shown in table 6.1 are used to model CSF in the simulations.

Table 6.1: Properties of CSF at human body temperature

Property	Symbol	Value	Unit
Temperature	T	37	°C
Density	$\rho$	993.3	$kg/mm^3$
Viscosity	$\mu$	0.6913	$mPa \cdot s$

### 6.1.2 CSF flow in rodents

As mentioned in section 2.3 and shown in figure 2.4 and 2.5 the flow of CSF has a pulsating nature. It can be seen that both the bulk flow velocity and the amplitude of the back-and-forth movement is relatively constant, which shows a lot of similarity to a sinusoidal wave. Therefore a simplified inflow profile of CSF can be constructed using a sinusoidal waveform with an amplitude of 20  $\mu m/s$  and an oscillating intensity of 10  $\mu m/s$  which is based on the measurements [29][27] performed on mice and can therefore be assumed to be realistic. The only remaining variable is the period of the sinusoidal. As mentioned before in section 2.3 the pulsating behaviour is synchronous with the heart rate and from figure 2.5 a heartbeat of 360 beats per minute can be derived for that particular animal, this is within the range of 310 to 840 beats per minutes which is the normative range for laboratory mice [54]. The resulting simplified inflow condition for rodents is shown in figure 6.1 over a period of one second.

### 6.1.3 CSF flow in humans

As the CSF fluid flow in the PVS is defined for the case of a mice brain the question now arises how to obtain this data for the human brain case. The measurements used to determine the flow in the mice brain have not been performed on humans, due to ethical limitations. However, if the CSF flow in the human brain can be quantified somewhere outside of the PVS and this same flow can be quantified in the mice brain a scaling factor can be calculated and used to relatively accurate predict the CSF flow in the PVS for the human brain. To obtain this scaling factor the CSF flow through the cerebral aqueduct is used. Within humans and mice the CSF volume flow through the cerebral aqueduct and its cross-sectional size is known, such that the CSF velocity can be determined in both cases. Therefore the ratio between CSF flow through the cerebral aqueduct and the PVS in mice is calculated such that this conversion factor can be used to obtain the CSF flow in the human cerebral aqueduct to the PVS.

The net CSF flow in the PVS of mice is known, therefore only the net CSF flow through the cerebral aqueduct is still needed to obtain the conversion factor. There are no direct measurements of this flow within mice, however by combining several other data the net flow can be obtained. Within the mice brain the CSF production is measured to be about 350 nanolitres per minute [55][56]. Due to the anatomy of the brain as shown previously in figure 2.1 the volume flow through the cerebral aqueduct is roughly equal to the total CSF production. The surface area of an intersection of the cerebral aqueduct in mice is determined to be on average about 0.15  $mm^2$  [57]. As a result the CSF flow velocity through the cerebral aqueduct is about 0.039  $mm/s$ . From section 6.1 we know that the CSF velocity through the PVS is measured to be about 0.02  $mm/s$ , therefore it can be said that the net CSF velocity through the PVS is about half that of the CSF velocity through the cerebral aqueduct.

As the conversion factor is known, the last unknown is the velocity flow of CSF through the cerebral aqueduct within the human brain. Research has been done on the volumetric net flow rate and direction of CSF in idiopathic normal pressure hydrocephalus within the human brain [58], however the interesting part for this thesis is the data from the control group of healthy subjects. The research showed a CSF volumetric net flow rate in the cerebral aqueduct of about 300 millilitres in 24 hours, which equates to about 0.2 millilitre per minute and corresponds to other research on this flow [55]. The surface area of the intersection of the cerebral aqueduct in men is determined in a research using magnetic resonance imaging (MRI) data to be about  $8 \text{ mm}^2$  [59]. Combining the volumetric flow and the surface area, the velocity of the CSF flow through the cerebral aqueduct in humans is determined to be about  $0.4 \text{ mm/s}$ . With the conversion factor obtained from the measurements in mice it can then be assumed that the net flow velocity of CSF in the human PVS is about  $0.2 \text{ mm/s}$ . From the same mice data the oscillatory movement is known to have an amplitude of half the net flow, which results in an oscillatory amplitude of the CSF flow in humans of  $0.1 \text{ mm/s}$ . The resting heart rate for humans varies between 60 to 100 beats per minute [60], in this thesis a resting heart rate of 60 is assumed. Using the determined values the simplified CSF velocity flow shown in figure 6.2 is obtained.

In table 6.2 a summary of the CSF flow in mice and human is presented. In the table the bold values are the calculated values whereas the other values are obtained from literature as explained in the previous paragraph.

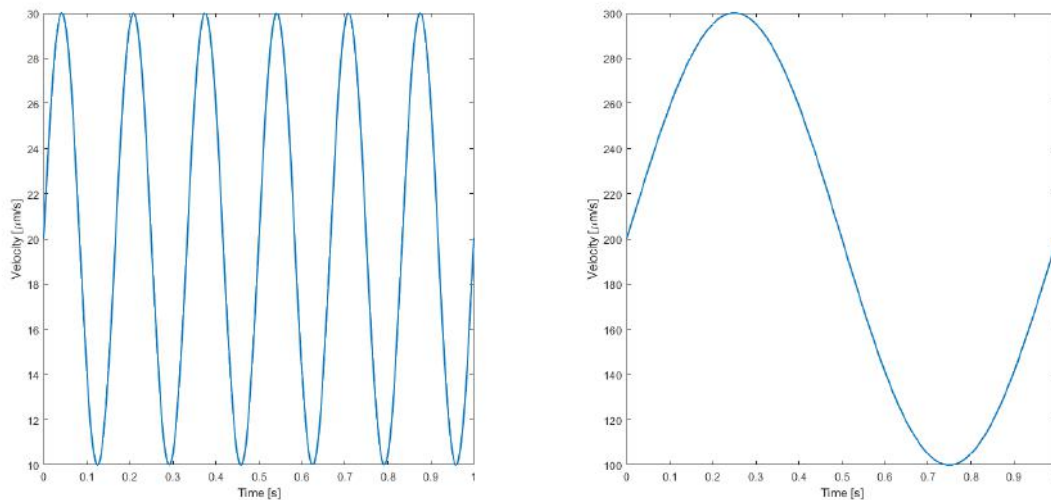


Figure 6.1: Simplified CSF velocity in mice Figure 6.2: Simplified CSF velocity in humans

Table 6.2: CSF flow comparison between mice and humans

Description	Mice quantity	Unit	Human quantity	Unit
CSF bulk flow PVS	20	$\mu m/s$	<b>0.2</b>	mm/s
CSF oscillating flow PVS	10	$\mu m/s$	<b>0.1</b>	mm/s
Heartbeat	360	bpm	60	bpm
CSF flow cerebral aquaduct	<b>0.039</b>	mm/s	<b>0.4</b>	mm/s
CSF production	350	nanolitres/minute	300	millilitres/day
Cerebral aquaduct size	0.15	$mm^2$	8	$mm^2$

## 6.2 Geometry and simulation setup

In this section the different geometries that are used in the simulation will be discussed and the simplifications that are made will be explained. The geometries for these simulations have to represent the area between the inner PVS wall and the outer artery wall. In section 2.2 a description of this area is already given, however in this section the quantified geometry will be presented.

First it should be noted that several simplifications are made to both the geometry and the simulation approach in general. The reasoning behind those simplifications is mainly to reduce the complexity in unnecessary parts. These simplifications are as follows:

- The walls are assumed to be static

Even though some researches suggest that a wavelike motion in the walls is the driving force of the CSF flow [27][30] this would complicate the simulations significantly.

- No elasticity is present in the walls

In the most realistic case artery walls will have some elasticity in them. However once again this would complicate the simulations significantly and it is isn't expected to make too much impact on the results.

- Gravitational forces are neglected

Gravitational forces are neglected in this case due to simplicity.

- Driving forces are reduced to an inlet flow

The driving forces of the CSF flow in the PVS are still up for debate, several researchers claim that a wavelike motion in the artery wall or rigid arterial motions have a part to play in the driving force. However, as this thesis is not interested in why the fluid moves, but is focused on how the fluid moves, the resulting fluid flow is obtained by inducing a velocity flow at the inlet of the geometry.

In this set of simulations the comparison is being made between three different geometries. The geometries are based on the research done in section 2.2 and are selected to cover most of the changes in cross-sectional area that have been found in the research. The geometries can be explained as a concentric annulus, a flattened elliptical shape and the same elliptical shape with an off-centred artery. The concentric annulus geometry serves multiple purposes, first of all it can be used as a benchmark case as the analytical solution for this shape has already been derived in section 5.2, but mainly it is chosen as the current computational studies all use this shape for their PVS and thus it can directly be compared to previous studies. The elliptical and flattened shape is based on the more recent findings that the PVS

shape is indeed flattened and elongated along the direction of the skull. The third geometry uses the same inner PVS wall as the elliptical and flattened shape, however in this case the artery is not centred, this has been shown to be more realistic, however the amount of displacement is difficult to determine, therefore an estimated value is taken in the geometries.

It is important that the results of the three different geometries are comparable. This is first of all done by keeping the length of the geometries the same, but the question remains what the dimensions of the flattened elliptical shape should be to keep it comparable to the concentric shape. In order to keep the flow behaviour in the various simulation comparable the Reynolds number will be matched, as shown in equation 6.1 the only parameter dependent on the geometry is the characteristic length  $L$ . This characteristic length is in the case of annular shaped regions the hydraulic diameter,  $d_h$ , which therefore will be matched between the different geometries. The calculation of the hydraulic diameter for the case of a concentric annulus is well known and shown already in the denominator of equation 5.2, but for clarity also shown in equation 6.2. The calculation for the hydraulic diameter of an annular ellipse is slightly more complicated as shown in equation [61]. It should be noted that in the case of an off centred artery the hydraulic diameter does not change.

$$\text{Re} = \frac{uL}{\nu} = \frac{\rho uL}{\mu} \quad (6.1)$$

$$d_{h,annulus} = d_{out} - d_{in} \quad (6.2)$$

$$d_{h_{ellipse}} = d_{ellipse,outer} - d_{in} \quad d_{ellipse,outer} = \frac{4wh(64 - 16e^2)}{(w+h)(64 - 3e^4)} \quad \text{with} \quad e = \frac{w-h}{w+h} \quad (6.3)$$

The size of the concentric annulus is determined in section 2.2 where it was stated that the typical radii of the artery is 0.3 mm and the size of the PVS is twice that large. Using the sizing of the concentric annulus the dimensions of the flattened elliptical shape can be determined using equations 6.3 and 6.2. There are however two unknowns, being the width and height of the ellipse, therefore a chosen value of 0.5 is assigned to the width. This is an arbitrary chosen value based on visual inspection. Keeping the width fixed at a value 0.5 mm and the hydraulic diameter at 0.6 mm, results in a height value for the ellipse of 0.77 mm. These values can be seen in table 6.3, where the values are linked to figure 6.3 for the concentric annulus and figure 6.4 for the non concentric annulus.

Table 6.3: Geometry parameters

Geometry shape	$r_1$ [mm]	$r_2$ [mm]	$r_3$ [mm]	x [mm]	y [mm]
Concentric	0.3	0.6	0.6	0	0
Flattened	0.3	0.77	0.50	0	0
Flattened + off-centered	0.3	0.77	0.50	0.15	-0.1

The setup of the simulation parameters is mostly the same as in section 5, where the fluid has the properties of CSF and the geometry of the artery itself is mimicking the PVS and is long enough to observe a fully developed flow. Furthermore a spatial step size,  $dx$ , of 0.009375 is chosen based on the grid convergence study performed in section 5 this was deemed to be accurate while still keeping the computational requirement manageable. In table 6.4 the simulation and some geometry parameters for this study are shown and in figure 6.5 the meshed geometries are shown.

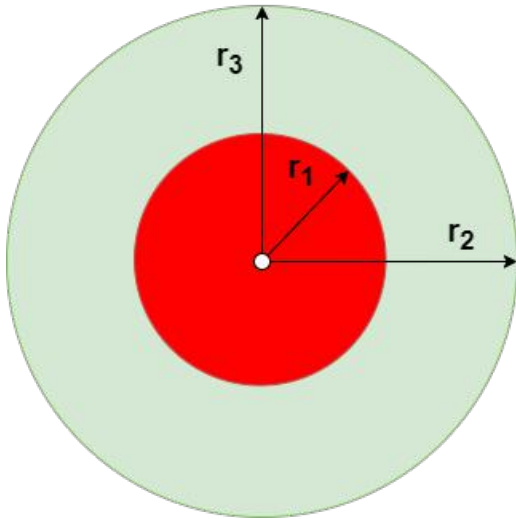


Figure 6.3: Geometry definitions for concentric annulus

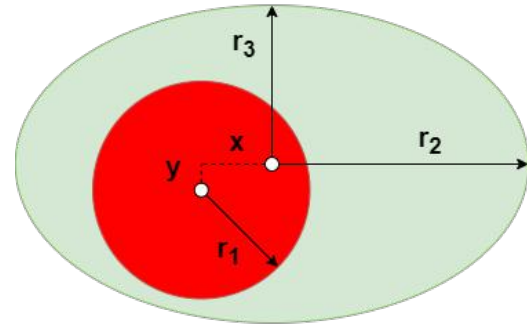


Figure 6.4: Geometry definitions for non concentric annulus

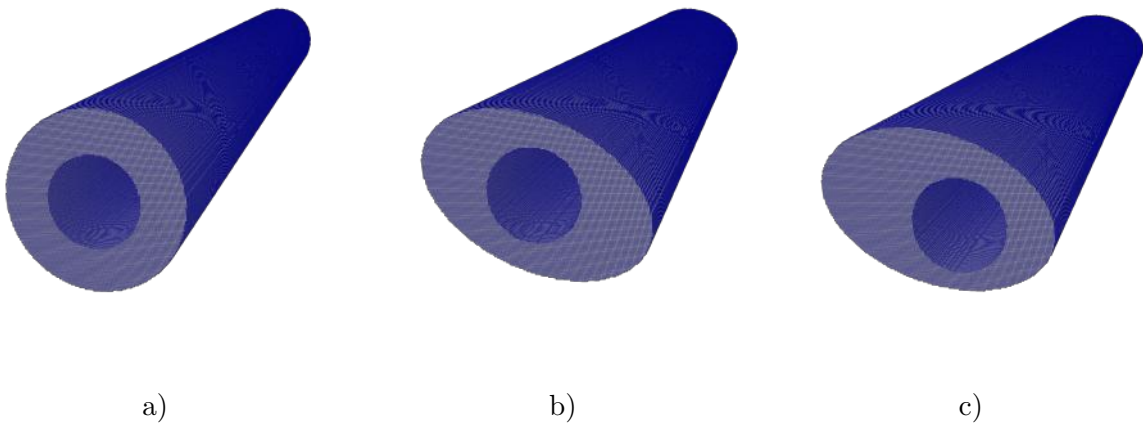


Figure 6.5: Meshed geometries of a) the concentric b) the flattened and c) the flattened and off-centered PVS

### 6.3 Analysis

The first simulation results are achieved by running fluid simulations on all three of the geometries shown in figure 6.5 over a time of six seconds using the velocity input shown in figure 6.1.3. In this section the results of these simulations are shown and the analysis of these results is presented.

First of all the velocity over time is compared between the different geometries. Obviously when taking the velocity over the entire cross-section the velocities for the different geometries are the same, as the inlet condition is the same and no leakage or fluid penetration of the walls is present in these simulations. Therefore the velocity over time is taken at the local maximum velocity nodes at a depth of 3 millimetre into the artery. The maximum velocity nodes are located in the centre of the largest open space in the cross-section and their coordinates are shown in table 6.5.

In figure 6.6 the fluid velocity at these nodes is plotted against the simulation time between

Table 6.4: Simulation parameters

Parameter	Value	Unit	Parameter	Value	Unit
Length	6	[mm]	Density	9.933E-7	[ $kg/mm^3$ ]
Hydraulic diameter	0.6	[mm]	Viscosity	6.913E-7	[ $kg/(mm \cdot s)$ ]
Grid spacing	0.009375	[mm]	Omega	1.6	[-]

Table 6.5: Maximum velocity nodes of the three geometries

Geometry shape	X [mm]	Y [mm]	Z [mm]
Concentric	0.69	0.26	3
Flattened	0.45	0.95	3
Flattened + off-centered	0.48	0.80	3

one and three seconds, which shows two pulsating cycles. The sinusoidal pattern with a period of a second is in accordance with the inflow condition equal to figure 6.1.3. The shape of the velocity pattern doesn't change between the geometries which is to be expected, the difference between the geometries however is the magnitude of the velocity. The off-centered geometry shows the highest fluid velocity whereas the concentric geometry shows the lowest velocity. These results are to be expected, as in the concentric geometry the fluid flow will be evenly distributed around the artery whereas in the off-centered geometry there won't be much flow in the small gap compared to the large gap.

To be able to confirm these assumptions several plots are made of the velocity profile of the cross-section of the different geometries. Two sets of plots are made, one at  $T_1$  and one  $T_2$ , which are respectively the minimum and the maximum of the sinusoidal and equal to  $t = 1.75s$  and  $t = 2.25s$ , as shown in figure 6.6 with vertical lines. At these time steps the velocity profiles are taken over a slice at  $z = 3$  for the different geometries. A three-dimensional representation of the different velocity profiles at  $T_1$  are shown in figure 6.7, 6.8 and 6.9, whereas the velocity profiles obtained at  $T_2$  are shown in figure 6.10 6.11 and 6.12.

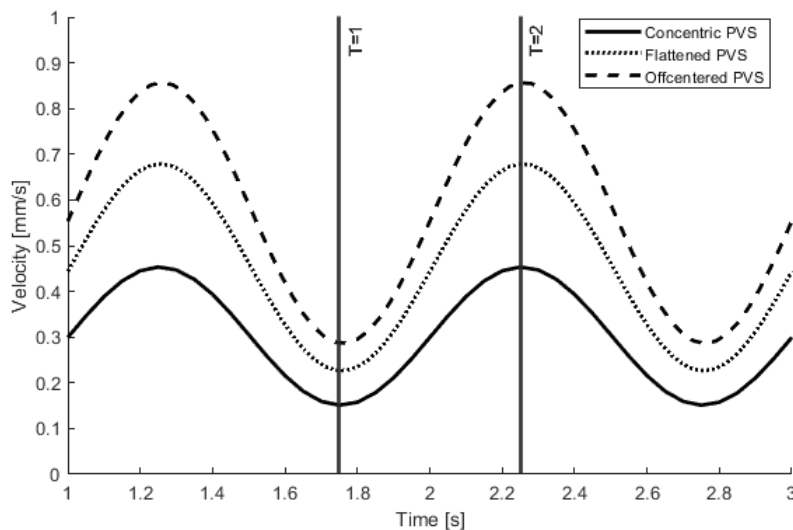


Figure 6.6: Velocity profile of maximum velocity node over time

As mentioned before the velocity profiles at time  $t = T_1$  show the flow distribution at the lowest velocity of the pulsating flow. The average velocity flow over the cross-sectional domain

at this time step is the same for each geometry, 0.1 mm/s, which is equal to the prescribed inflow condition.

The geometry with the concentric PVS shape is shown in figure 6.7 and shows the same shape as was seen during the preliminary studies in section 5. This is to be expected as the fluid velocities in this simulation once again aren't high enough for the flow to leave the laminar region, more specifically the local Reynolds number is approximately 0.13 in this geometry with a maximum local velocity of 0.15 mm/s. When comparing the velocity profile of the concentric geometry to the flattened geometry in figure 6.8 it can be seen that the uniformly distributed flow shifts to a two stream dominated flow. The flattened geometry shows very little flow in the small gaps and two major flows in the large gaps with velocities reaching up to 0.22 mm/s. In the case with the off-centered artery shown in figure 6.9 it can be seen that the flow is dominated in the large gap, whereas around the rest of the artery the space of the PVS is very small and thus limited flow is present. The main flow in this case reaches velocities up to 0.28 mm/s.

In table 6.6 the maximum velocities present in the different geometries at time  $t = T_1$  are shown in the second column. When comparing the relative differences between the velocities taking the concentric geometry as the base the local velocity in the flattened geometry is almost 1.5 times as high and the off-centered geometry almost twice as high. This increase in velocity is to be expected due to the fact that the effective diameter over the part of the geometry with the largest velocity is greater for the flattened and off-centered cases.

The velocity profiles taken at time  $t = T_2$  are very similar to those taken at time  $t = T_1$ . In these simulations the inlet velocity is pulsating and not oscillating, therefore no directional changes of the flow are seen and only magnitude differences are present between the two time steps. As can be seen in figure 6.10, 6.11 and 6.12 once again the concentric geometry shows a evenly distributed flow around the artery, the flattened geometry results in two flows in the larger open bodies of the geometry and the off-centered artery results in a dominant flow in the large open gap with very little flow around the rest of the artery.

The average magnitude of the flow velocity at this time step is for each of the geometries about 0.3 mm/s which is equal to the inlet velocity. The local velocities however once again change significantly, in the concentric geometry fluid velocities up to 0.45 mm/s are reached, whereas in the flattened geometry the flow reaches velocities up to 0.68 mm/s and in the off-centered geometry the highest velocity is reached at 0.85 mm/s. These velocities are shown in table 6.6 in the third column, once again the same relative increases compared to the concentric geometry are seen, being 1.5 times for the flattened and almost 2 times for the off-centered geometry. Even though the local velocities are significantly higher than those at  $t = T_1$  the local Reynolds number does not exceed a value of 1, which results in laminar flow and thus explains the same flow profiles for both time steps.

Table 6.6: Maximum velocities and relative differences

Geometry shape	$T_1$ Velocity [mm/s]	$T_2$ Velocity [mm/s]	Relative increase Compared to concentric [%]
Concentric	0.151	0.453	100
Flattened	0.227	0.679	~150
Flattened + off-centered	0.287	0.856	~190

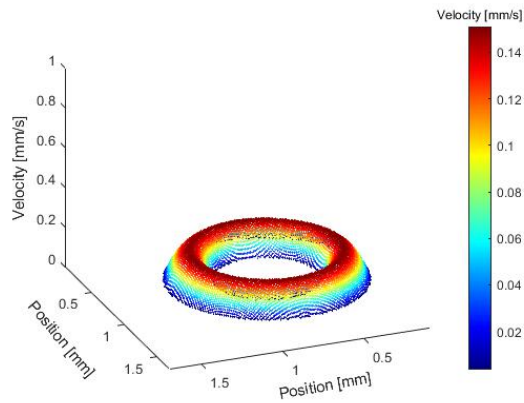


Figure 6.7: Velocity profile of concentric PVS at time =  $T_1$

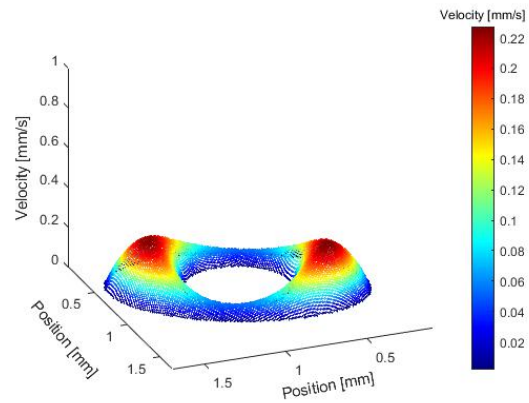


Figure 6.8: Velocity profile of flattened PVS at time =  $T_1$

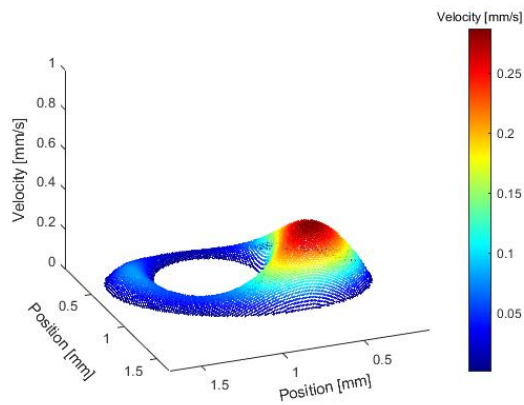


Figure 6.9: Velocity profile of offcentered and flattened PVS at time =  $T_1$

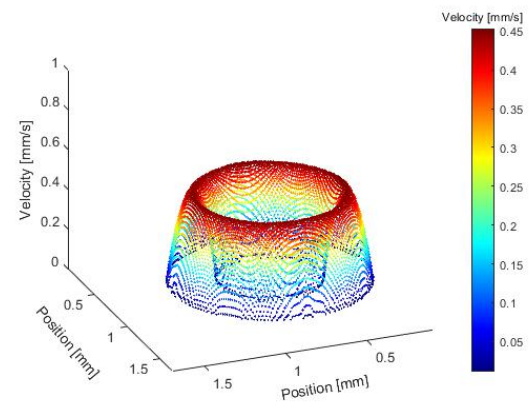


Figure 6.10: Velocity profile of concentric PVS at time =  $T_2$

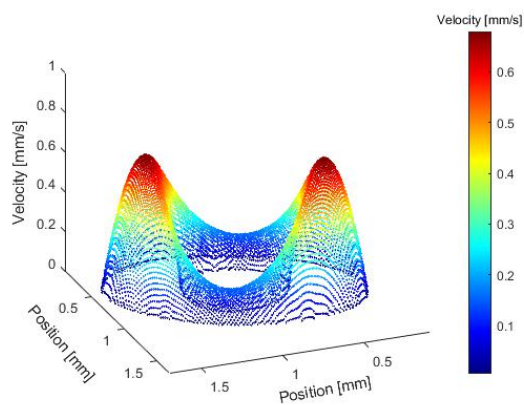


Figure 6.11: Velocity profile of flattened PVS at time =  $T_2$

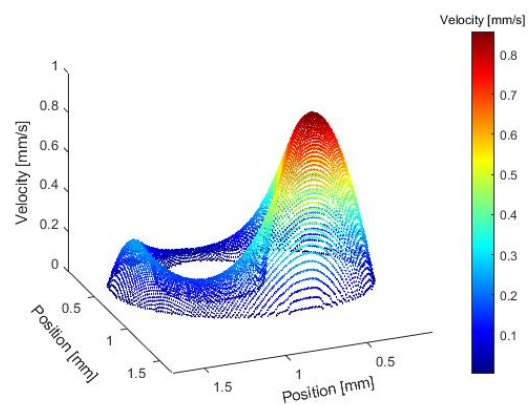


Figure 6.12: Velocity profile of offcentered and flattened PVS at time =  $T_2$

## Chapter 7

# Geometry change effect on previous studies

As shown in section 6 the cross-sectional PVS shape significantly influences the shape of the velocity profile and the local velocity magnitude in the PVS. In section 1 it was already mentioned that most of the current computational research regarding CSF flow in the PVS is limited to concentric PVS shapes. Therefore in this section a comparison study is done to directly investigate the effect of the PVS shape on previous research's output.

The paper used for this comparison analysis is the research performed by Daversin-Catty et al. [30]. In this research the mechanisms behind perivascular fluid flow are studied using a concentric shaped PVS around a geometry of a bifurcating artery. After studying the paper and its conclusions the question arises whether the cross-sectional shape of the PVS is the solution to some of the conclusions that were drawn. Therefore in this set of simulations a simplified version of the performed simulations are done using the same simulation parameters and geometry specifications to reproduce the result for the concentric case and add the comparison with a flattened and off-centered geometry. The comparison between the three simulations will then be used to discuss the conclusions drawn in the paper and determine whether or not the cross-sectional shape is the solution or not.

In this chapter first more details regarding the research and the aforementioned conclusions are given in section 7.1. Then the simulation parameters are given in section 7.2 with the details regarding the parameters to reproduce the paper's results. Finally in section 7.3 the results of the three simulations are discussed and the conclusions are drawn.

### 7.1 Details of the research

As mentioned the paper is a computational study to determine the mechanisms behind the CSF flow in the PVS in mice. In the paper the measurements done by Mestre et al. [27] and Bedussi et al. [29], which have been previously mentioned in section 2, are used reference net and oscillatory movement. The researchers generated the geometry starting from a model representation of a cerebral artery. This model was scaled down to mice size and the PVS was defined by creating an annular cylinder surrounding the artery with the artery wall as its inner surface. The width of the PVS was set proportional to the arterial diameter, which is the same assumption as has been made in section 6, which resulted in PVS widths from 28-42 micrometer and inner arterial diameters of 32-46 micrometer. The mesh of the

resulting geometry is shown in figure 7.1.

To be able to achieve the desired flow velocities seen in measurements the paper compares a total of seven different combinations of forces. The results of these different force combinations are irrelevant for the purpose of this thesis, therefore only the relevant forces and the computational model with the best results will be discussed here. First of all there is the oscillatory component of the flow which is in-phase with the heartbeat. This flow is driven by pulsatile arterial wall motions, which occur due to the arterial blood flow pulsating in the artery. However, with only this force acting on the fluid an oscillatory movement is achieved, but no net flow. Therefore a pressure gradient is added to the model. Several sources and thus magnitudes of the pressure gradient were tested, but a pressure gradient induced by the cardiac cycle achieved the most accurate results. The resulting time profile of the average velocity at the inlet can be seen in figure 7.2 by the yellow line for the relevant case, where negative values correspond to downward flow (which is in the direction of the blood flow).

Comparison of the results of this computational study with the experimental results of Mestre et al. [27] and Bedussi et al. [29] results in two major differences:

- First of all the average peak-to-peak velocity amplitude is higher in the computational study compared to the experimental results.
- Secondly in order to achieve the measured net velocities in the experimental studies the upper values of static pressure gradients have to be added to the computational model.

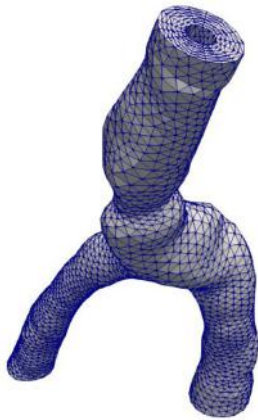


Figure 7.1: PVS mesh[30]

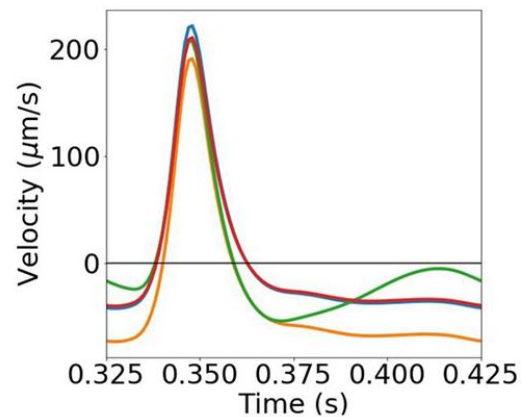


Figure 7.2: Resulting velocity profile (Yellow for comparison case)

## 7.2 Simulation parameters

In this study the simulation performed by Catty et al. [30] is redone using three different cross-sectional shapes with the purpose of investigating whether this change in setup solves the differences found between the computational study done and the measurements by Mestre et al. [27] and Bedussi et al. [29]. In order to perform the simulation several simplifications are made, as those details are not of relevance in this study.

First of all a simplified version of the geometry shown in 7.1 is used. The sizing of the geometry is kept the same, however instead of the complex shape shown a straight artery is

used similar to those shown in chapter 6. Once again three geometries are being evaluated with different cross-sectional shapes, being a concentric annulus, a flattened PVS and a flattened PVS with an off-centered artery location. In order to match the simulations performed in the paper the length of the PVS is set at 1 millimetre and the PVS width and inner arterial diameter are set at the same length of 40 micrometre for the concentric case. The dimensions of the flattened and the flattened and off-centred case are calculated with the same process as discussed in section 6.2. The resulting specifications for the geometry are shown in table 7.1, where the numbers are once again matched with figure 6.3 and 6.4. Due to the direct scaling down of the case used in the previous chapter the same mesh convergence study can be used, therefore as shown in section 5 once again a total of 31 elements are used in the vertical direction of the concentric case. The meshed geometries are shown in figure 7.3 for a cross-sectional slice. Furthermore the fluid properties, such as viscosity and density, are matched to the paper and shown with the rest of the simulation parameters in table 7.2.

Table 7.1: Geometry specifications for comparison case

Geometry shape	r1 [mm]	r2 [mm]	r3 [mm]	x [mm]	y [mm]
Concentric	0.02	0.04	0.04	0	0
Flattened	0.02	0.05133	0.0333	0	0
Flattened + off-centered	0.02	0.05133	0.0333	0.01	-0.00667

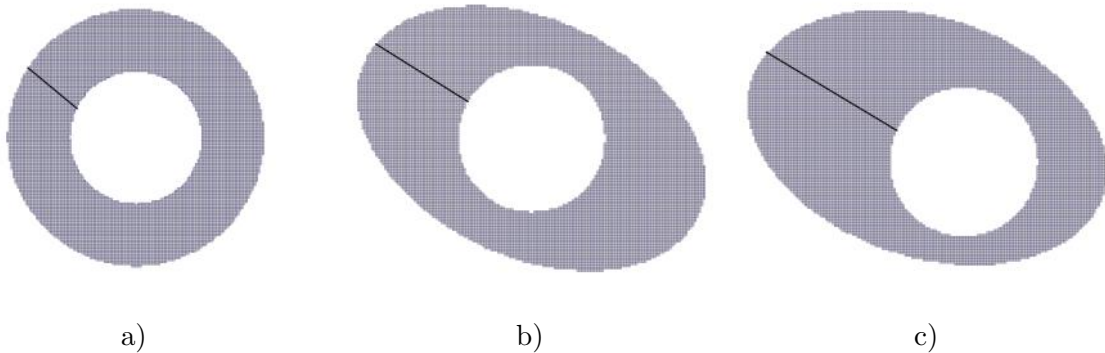


Figure 7.3: Meshed cross-sectional geometries of a) the concentric b) the flattened and c) the flattened and off-centered PVS for the comparison simulation study

Table 7.2: simulation parameters

Parameter	Value	Unit	Parameter	Value	Unit
Length	1	[mm]	Density	10E-7	[ $kg/mm^3$ ]
Hydraulic diameter	0.02	[mm]	Viscosity	6.97E-7	[ $kg/(mm \cdot s)$ ]
Grid size	0.00064	[mm]	Omega	1.6	[-]

To be able to achieve the same flow in the PVS without having to implement the forces mentioned in section 7.1 the inlet velocity in these simulation is matched to the resulting velocity of the paper. This does mean that the arterial wall is static in these simulation, instead of having the arterial wall pulsations which are used in the paper. Therefore the streamlines of the simulations in this case will be straight lines, but this does not influence the magnitude differences which are required to answer the questions in this study. The time profile of the average velocity shown in figure 7.2 is quantified, resulting in the velocity over time profile shown in figure 7.4.

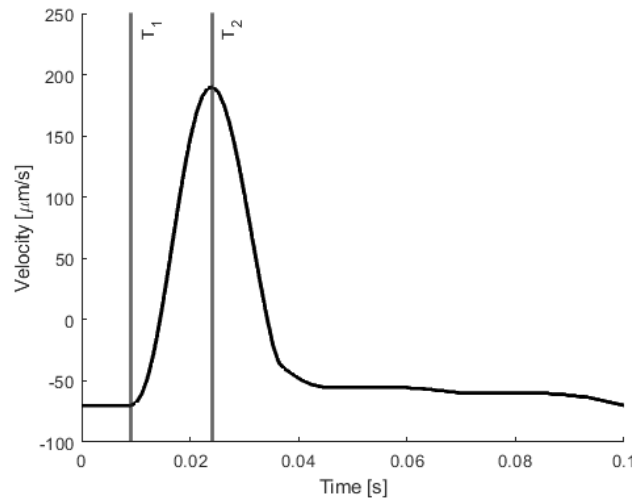


Figure 7.4: Quantified inlet velocity of comparison study

### 7.3 Analysis

To be able to answer the question stated in section 7.1 several aspects of the geometry are analysed. First of all the velocity profile plots at two time steps are shown and compared to be able to analyse the general flow profile. Then the fluid velocity for the main flowing region in the geometry is analysed over time and lastly an estimated plot for the microsphere position over time is constructed and compared.

First of all the velocity profiles at two time steps are shown, the maximum downstream velocity and the maximum upstream velocity. These time steps are indicated in figure 7.4, with the maximum downstream velocity shown as  $T_1$  at 0.009 seconds and the maximum upstream velocity shown as  $T_2$  at 0.024 seconds. In figure 7.8 to 7.13 the velocity profiles are shown for all three geometries at both time steps. As the geometry between this study and the simulation performed in section 6 are the same the velocity profiles show identical shapes. In this case however the flow changes direction which is clearly visible when comparing the two time steps. In the concentric case a clear laminar parabolic poiseuille-like flow profile is shown, which verifies the simulations as this is to be expected for simulations with such low Reynolds numbers. As is the case in the previous study shown in chapter 6 adjusting the geometry to a flattened PVS case increases local velocity in the two larger open regions. Moving the artery results in a clear distinction between the main flowing region and slower creeping flow regions in the rest of the geometry.

Secondly the average fluid velocity over time is being compared and analysed. This is done by taking the average fluid velocity over a line through the largest open area in the geometry as indicated in figure 7.3 by the black lines. The average velocity over the entire cross-section is the same for each of the geometries, however the average fluid velocity over this line does change. In the measurements performed by Mestre et al. [27] and Bedussi et al. [29] it is mentioned that microspheres that got stuck and stopped moving weren't taken into account. Therefore it can be assumed that the microspheres that were taken into account during the measurements would for the majority be flowing in the largest open area of the geometry, as the microspheres in the small gaps would more easily get stuck. The result is shown in figure 7.5 in which all three geometries are shown in one diagram. As can be seen in the concentric case the average velocity is identical to the velocity obtained in the paper by Catty et al. [30]

as shown in figure 7.2 which is to be expected and thus verifies the simulation parameters. It can then be seen that the average velocity over the main flowing gap of the geometry increases for the other two geometries, both the maximum upstream velocity increases as well as the steady downstream velocity. As such the peak-to-peak velocity in this region increases as well.

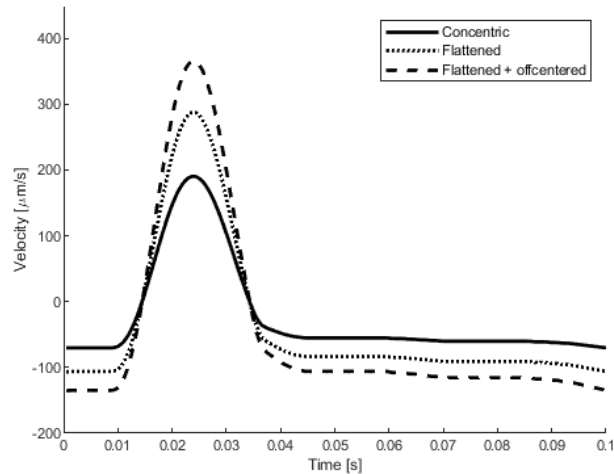


Figure 7.5: Average fluid velocity over time

In figure 7.7 the resulting position plot of particles released at the inlet of the simulation performed by Catty et al. [30] is shown, where the yellow line is the model which this studies compares to. Therefore an estimated microsphere position plot is made using the average velocity over time plot as shown in figure 7.5. By multiplying the fluid velocity with the temporal time step size the expected movement of a microsphere which is to be released in the PVS is obtained. In figure 7.6 the position plot is shown over 0.5 seconds of simulation time, which can therefore be compared to the result obtained in the paper shown in figure 7.7. The result of the concentric case should be identical to the result in the paper, however in this case it can be seen that there is a discrepancy between the two. In the paper the microsphere reaches a downstream position of 15 micrometre after 0.5 seconds, whereas in the performed simulation in this study the position is about 11 micrometre downstream. This difference is caused by a slight inaccuracy in the quantification of the velocity over time data from the paper to the input velocity of the simulation model used in this thesis. However since the oscillation of the microsphere is almost identical and the flow is highly laminar this discrepancy should not influence the statements made in this thesis. As is to be expected based on the average fluid velocity over time plot it can be seen that for the flattened and the off-centred case both the oscillation and the net downstream velocity increases.

Recalling the question stated in the introduction of this chapter in section 7.1, whether or not changing the cross-sectional shape of the PVS is the solution to the too high peak-to-peak velocity amplitudes and the too high required forces. First of all the peak-to-peak velocity, in figure 7.5 the development of fluid velocity over time is shown from which the peak-to-peak velocity can be derived. In table 7.3 the maximum downstream and upstream velocity of all three geometries is stated with the resulting peak-to-peak velocity amplitude. As can be seen, rather than reducing the peak-to-peak velocity amplitude it is only increased. In figure 7.6 however it can be seen that when assuming that the majority of microspheres will move through the largest and fastest flowing region of the geometry the net and oscillating

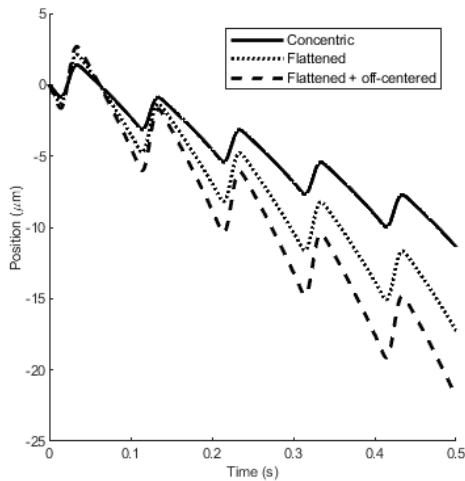


Figure 7.6: Estimated microsphere position plot over 0.5 seconds

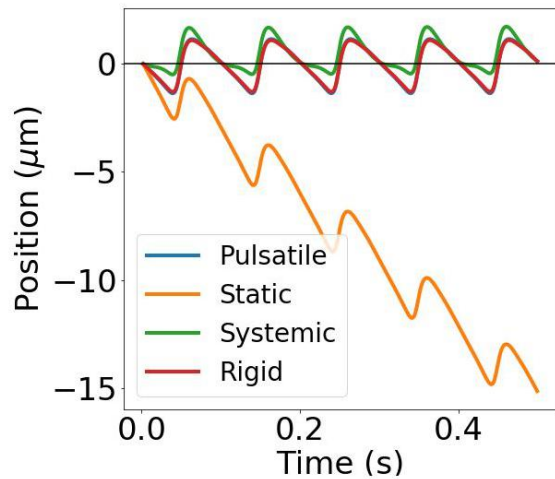


Figure 7.7: Position plots of particles obtained by Catty et al. [30]

movement increases significantly. In table 7.4 it is shown that the net movement of the microspheres is about 1.5 times as high for the flattened shape compared to the concentric shape, whereas the offset of the artery even increases the movement to twice as high as the concentric case. Therefore it can be said that most likely lower forces can be applied to the fluid, which are more in the reasonable range, while still achieving the movement patterns described by Bedussi et al. [29] and Mestre et al. [27].

Table 7.3: Peak-to-peak velocity analysis of the simulations

Geometry shape	Max downstream [ $\mu\text{m}/\text{s}$ ]	Max upstream [ $\mu\text{m}/\text{s}$ ]	peak-to-peak [ $\mu\text{m}/\text{s}$ ]
Concentric	70	190	260
Flattened	107	287	394
Flattened + off-centered	135	365	500

Table 7.4: Estimated net and oscillatory movement of microspheres

Geometry shape	Net flow [ $\mu\text{m}/\text{s}$ ]	Oscillating movement [ $\mu\text{m}/\text{cycle}$ ]
Comparison paper	30	2
Concentric	22.6	2
Flattened	34.4	3.3
Flattened + off-centered	43.6	4.3

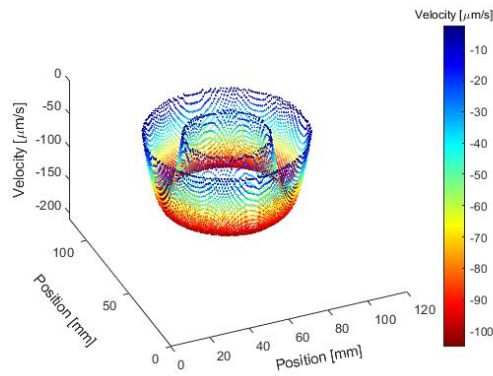


Figure 7.8: Velocity profile of concentric PVS at time step  $T_1$

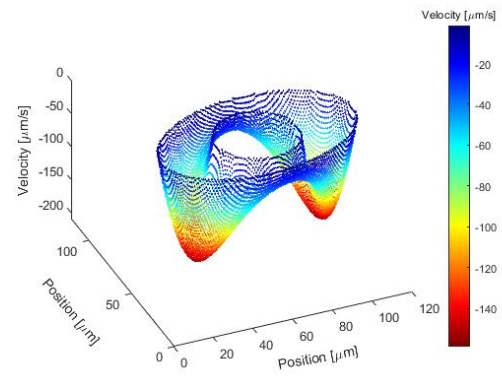


Figure 7.9: Velocity profile of flattened PVS at time step  $T_1$

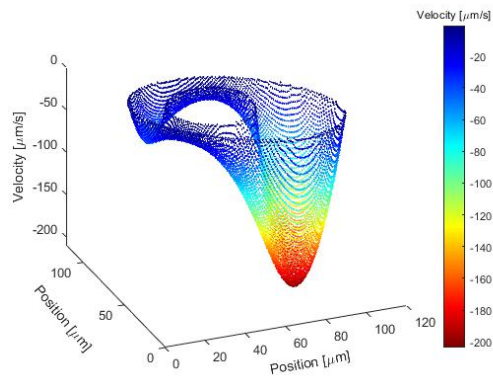


Figure 7.10: Velocity profile of off-centered and flattened PVS at time step  $T_1$

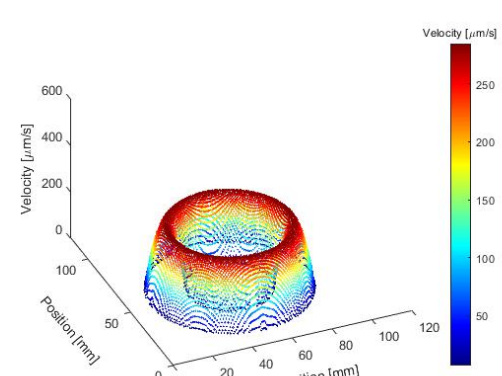


Figure 7.11: Velocity profile of concentric PVS at time step  $T_2$

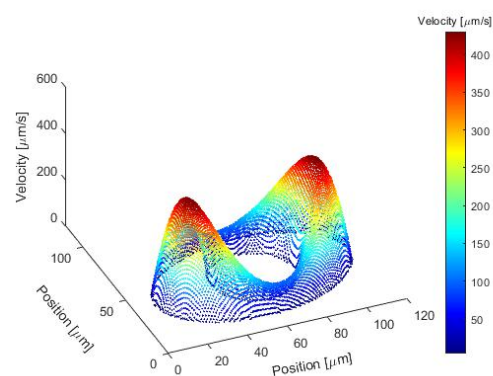


Figure 7.12: Velocity profile of flattened PVS at time step  $T_2$

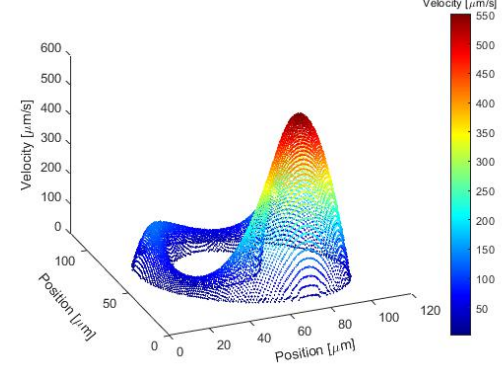


Figure 7.13: Velocity profile of off-centered and flattened PVS at time step  $T_2$

## Chapter 8

# Realistic artery study

In the previous chapters the CSF flow behaviour is simulated and analysed in straight arteries with three different cross-sectional shapes. The effect of the changes in cross-sectional shapes have been analysed and compared to previously published studies. However the question that arises is whether these findings are also valid for more complex and realistic shapes of the artery and PVS. Therefore a third set of simulations is performed using a realistic artery geometry around which the PVS is constructed.

Using the realistic artery geometry will introduce several new aspects to the simulation, being a bifurcation of the artery, several complex and tight corners of the artery as well as an artery wall with varying diameter. The tight cornering does however also limit this study in some extent. In the previous simulations three different cross-sectional shapes for the PVS were used, a concentric, a flattened and an off-centered flattened shape. Due to the tight cornering present in this artery and the size of the PVS the flattened shape with an off-centered artery can't be constructed as will be explained in section 8.1. Therefore only the concentric and flattened shape are used in this study. In general the same simulation parameters are used as in the previous studies such that the results can be compared.

In this chapter first the construction of the geometry and the simulation parameters are discussed after which the results of the simulations are shown and analysed.

### 8.1 Geometry

As mentioned in the introduction the geometry of the PVS is based on the geometry of a realistic artery which is shown in figure 8.1. It is a visualisation of an artery present in the brain, however it contains more small arteries than is usually seen in pial arteries which this thesis is interested in. Therefore the artery is slightly altered by removing the small bifurcations seen at the top of the geometry, such that only the core artery is left as shown in figure 8.2. The resulting geometry is a realistic artery shape with varying diameter over the length, containing a bifurcation as well as several complex corners.

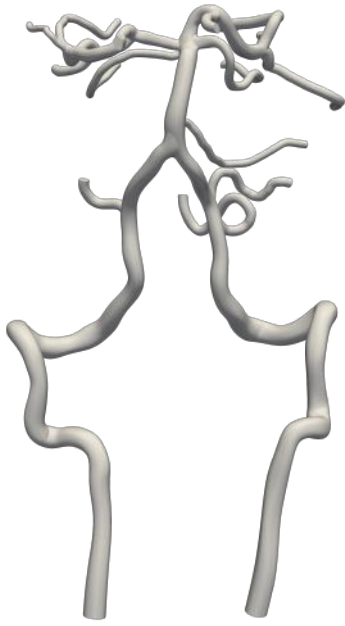


Figure 8.1: Full artery model

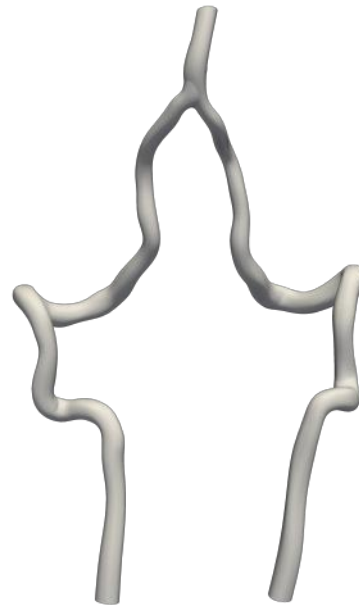


Figure 8.2: Reduced artery model

The vertical length of the model is about 10 millimetres and the diameter of the artery varies between 0.4 and 0.5 millimetre. Therefore the PVS should have a diameter of somewhere between 0.8 and 1 millimetre for the concentric case as this is double the size of the artery, in these simulations a constant diameter of 0.85 millimetre is chosen for the concentric PVS. The size of the flattened geometry is once again selected based on the procedure described in section 6.2. The resulting geometry specifications are shown in table 8.1, where the numbers are once again matched with figure 6.3 and 6.4.

Table 8.1: Geometry definitions for the realistic artery study

Geometry shape	$r_1$ [mm]	$r_2$ [mm]	$r_3$ [mm]
Concentric	0.2-0.25	0.425	0.425
Flattened	0.2-0.25	0.35	0.56

The PVS is constructed around the artery model using the 3d CAD design software *SolidWorks*. First the centre line of the geometry is constructed, such that the PVS shapes can then be drawn over this line. However, the exact centre line of the geometry can't be used as this would result in the PVS intersecting itself. This problem occurs due to the size of the PVS and the tight corners. As the size of the PVS can't be adjusted this problem is solved by relaxing the centre line in the the corners, as increasing the radius of the corners makes it possible for the PVS shapes to follow the line. This does however mean that the artery is not exactly in the centre of the PVS in most of the geometry, but the location of the artery with respect to the PVS is the same for both cross-sectional shapes and thus no significant problem is expected as a result of this. The geometry with the artery and the PVS and the artery is shown in figure 8.3 and 8.4 for respectively the concentric and the flattened PVS model.

The geometries in this study are of the human brain size and therefore almost identical to the sizes in the simulations performed in section 6. As a result the grid convergence

study, as shown in section 5, can once again be used to determine the spatial step size and thus  $dx = 0.009375$  is used for the simulations. This spatial step size is sufficient for an accurate solution, but still limiting the required computational power. In figure 8.5 and 8.6 the meshed geometries of respectively the concentric and the flattened geometry are shown in which the inlet is located at the top and the outlet located at the bottom of the geometry.

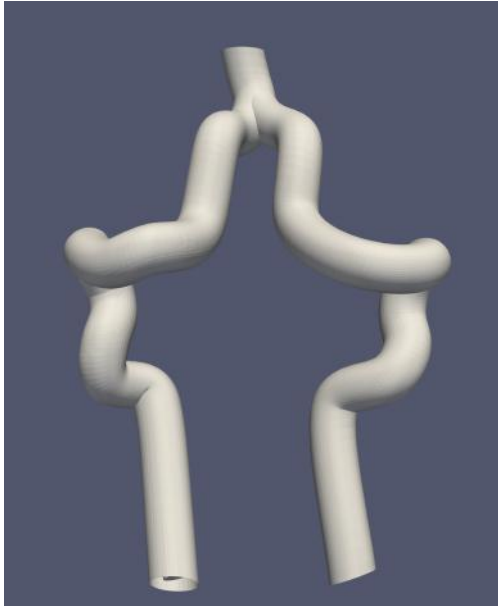


Figure 8.3: Concentric PVS model

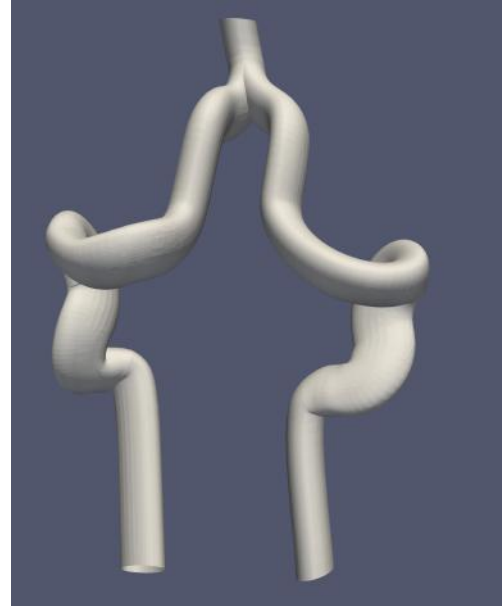


Figure 8.4: Flattened PVS model

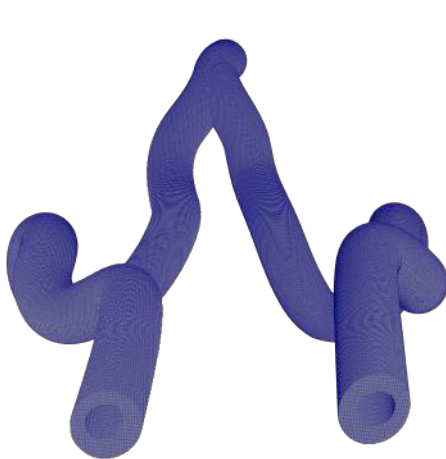


Figure 8.5: Meshed geometry of the concentric PVS model

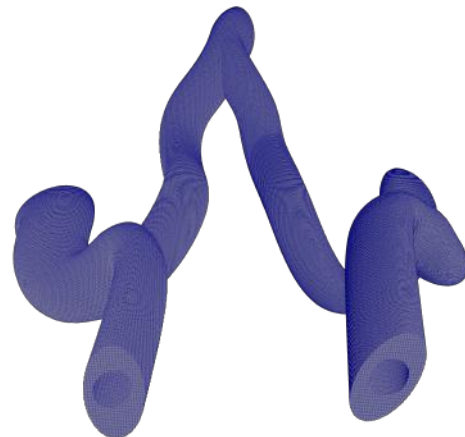


Figure 8.6: Meshed geometry of the flattened PVS model

## 8.2 Simulation parameters

In these simulations the CSF flow in the human brain is once again simulated, which is the same setup as the simulations performed in chapter 6. Therefore most of the simulations parameters are identical to that study as can be seen in table 8.2. In this section a new inlet velocity will be created for this set of simulations.

Table 8.2: Simulation parameters study 3

Parameter	Value	Unit	Parameter	Value	Unit
Length	10	[mm]	Density	10E-7	[kg/mm <sup>3</sup> ]
Hydraulic diameter	0.45	[mm]	Viscosity	6.97E-7	[kg/(mm · s)]
Grid size	009375	[mm]	Omega	1.6	[-]

This study uses the same inlet velocity profile as described in chapter 7. In that study however, the CSF flow in a mice was modelled, therefore the inlet velocity profile has to be scaled to the human brain size for this set of simulations. The main difference between CSF flow in the human and mice brain is the oscillation frequency and the magnitude. The heart rate of a human at rest is about 60 beat per minutes, whereas the heart rate of a mice is between 500 and 700 beat per minute, so roughly 10 times faster than humans [62]. As the heart rate is directly linked to the oscillation frequency this means that instead of a cycle of 0.1 seconds, which was the case in chapter 7, a cycle of 1 second is used here. Furthermore the CSF velocity in the human brain is higher than in mice brains, which in section 6.1.3 and table 6.2 was shown to be about 10 times as large. As a result the inlet velocity profile shown in figure 8.7 is used for the simulations.

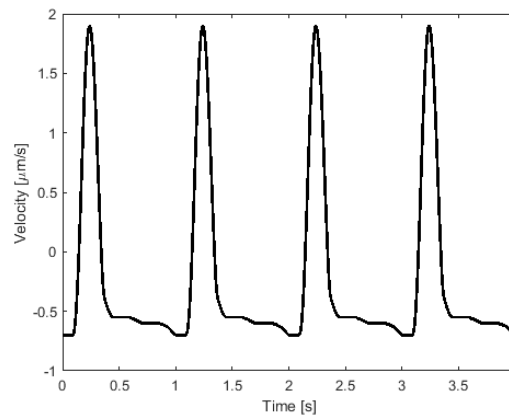


Figure 8.7: Inlet velocity profile study 3

## 8.3 Analysis

The aim of this simulation is to analyse and compare the behaviour of the CSF flow in the two different PVS shapes. To be able to get a full understanding of the behaviour of the flow several different approaches to the analysis have been performed. First of all the velocity profile over different slices in the geometry have been plotted and compared to be able to get a global understanding of how the fluid flows through the PVS. Then the flow has been visualised using streamlines and glyph plots at different time steps, such that the development of the flow over time can be seen. Last but not least the fluid velocity of nine points

throughout the geometry have been plotted over time to be able to analyse and compare the exact development of the flow in these points over time.

When taking a closer look at the geometry there is a decent amount of symmetry visible through which the fluid flow will behave roughly the same. Therefore by focusing the analysis on certain regions the analysis can be done more in depth, while still achieving the same amount of completeness. For the analysis using the geometry slices, the streamlines and the glyph plots the focus is on the bifurcation region and the region containing the right cornering, the cutout of these regions can be seen in respectively figure 8.8 and 8.9.

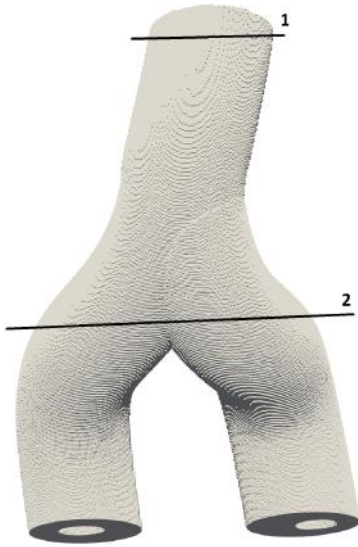


Figure 8.8: Meshed geometry of bifurcation section with indicated slices

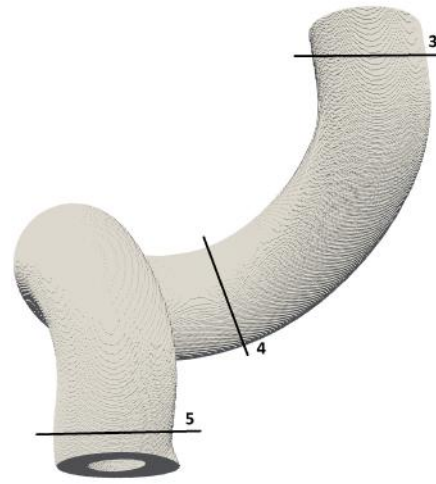


Figure 8.9: Meshed geometry of right cornering section with indicated slices

### 8.3.1 Velocity profile slices

First of all the velocity profile slices will be discussed. These are used to show the general flow shape of the fluid flow in the PVS. A total of 5 slices are made, two of which are located in the bifurcation region and the other three are located in the right cornering region of the geometry. In figure 8.8 and 8.9 the slices are indicated by black straight lines and labelled with a number and in table 8.3 the coordinates of the different slices are given. The slices are taken at a time of  $t = 2.28$  seconds, which is just after the peak in downward velocity flow as can be seen in figure 8.7. This time step is selected due to the high fluid velocities present in the geometry at this time step, such that the range of velocities is larger and better for analysing purposes.

Table 8.3: Coordinates of velocity profile slices

	Origin			Normal to		
	X [mm]	Y [mm]	Z [mm]	X [mm]	Y [mm]	Z [mm]
Slice 1	3.5	2.9	0.45	-0.05	0.0265	1
Slice 2	3.5	2.9	1.8	0	0	1
Slice 3	2.55	1.3	3.9	-0.4	-0.6	0.7
Slice 4	1.3	1.3	4.5	1	-0.2	-0.05
Slice 5	1.64	1.31	5.3	0.014	-0.2	1

The bifurcation of the sole artery into two separate arteries is an interesting part of the arteries geometry as the flow will be divided over both arteries in this region and directly behind the bifurcation a new void region occurs. To analyse this behaviour two slices are located in this region, one in front of the bifurcation close to the inlet of the geometry and one right after the bifurcation. The figures of the velocity profiles of these slices for both geometries are shown in figure 8.10. It should first be noticed that the velocity profiles of slice 1, figures 8.10a and 8.10c, are very similar to the results of the first study performed in chapter 6. This is to be expected as this part of the geometry still closely resembles a straight artery. As such these velocity profile slices can be used as a good validation for the simulation. It should however be noticed that in both geometries the velocity in the upper half of the cross section is higher than in the bottom half, this can be explained by the fact that the geometry is slightly angled downwards whereas the inlet velocity is injected horizontally.

When evaluating the slices just after the bifurcation, figures 8.10b and 8.10d, a more unexpected results is seen. This part of the geometry is quite significantly angled downward and it should be noticed that the slice is not taken exactly normal to the artery, as the cross-sectional shape of the artery seen here is elongated. In this slice the shape of the PVS is also more similar between the two geometries than expected, however also some clear differences can be seen. First of all the similarities, in both geometries the bulk of the flow is in the top region of the slice, which is due to the fact that the artery is angled downwards and thus the CSF flow is also pushed downwards. It is also clear that in the void region just behind the bifurcation, in these slices this is the region between the two arteries, almost no flow is present in both geometries. Furthermore the maximum flow velocity is almost identical between both the geometries, which compared to the velocities seen in slice 1 is a significant difference. The difference can be seen in the upper region of the slice, where in the concentric geometry a higher flow velocity is angled into the left artery compared to the flattened case. However, in both geometries the bulk flow is directed in the right artery, which is to be expected due to the direction of the artery as seen in figure 8.2.

In the right cornering section of the geometry three slices are taken for the velocity profile analysis. These slices are taken after each of the corners to be able to see how the flow moves through those corners and what the differences and similarities in this region are between the two geometries. It should be mentioned that all slices are shown viewed from the inlet side of the geometry towards the outlet of the geometry, in figure 8.11 the different velocity profile slices are shown.

As can be seen the distribution of the flow around the artery is significantly influenced by the cornering. The first slice, shown in figure 8.11a and figure 8.11d, is located in the beginning of a vertical descend of the artery. This is clearly visible in the velocity profile slices by the dominant velocity flow in the region above the artery and shows similar results for both the concentric and flattened geometry. Even though the flow in the flattened geometry is dominant in the region above the artery, below the artery there is still a flow present of about 1.4 mm/s which is about 60% of the velocity seen in the region above the artery. In the concentric geometry however velocity in the region below the artery reach only up to 0.4 mm/s which is about 30% of the velocity seen in the region above the artery.

The second slices in the cornering section, shown in figures 8.11b and 8.11e, are located after a right bend of the artery. This is can be seen in the velocity profile slices as the flow is most dominant in the top left side of the geometry. However contrary to the first slices a more similar distribution of the flow is seen between the two geometries as both show only

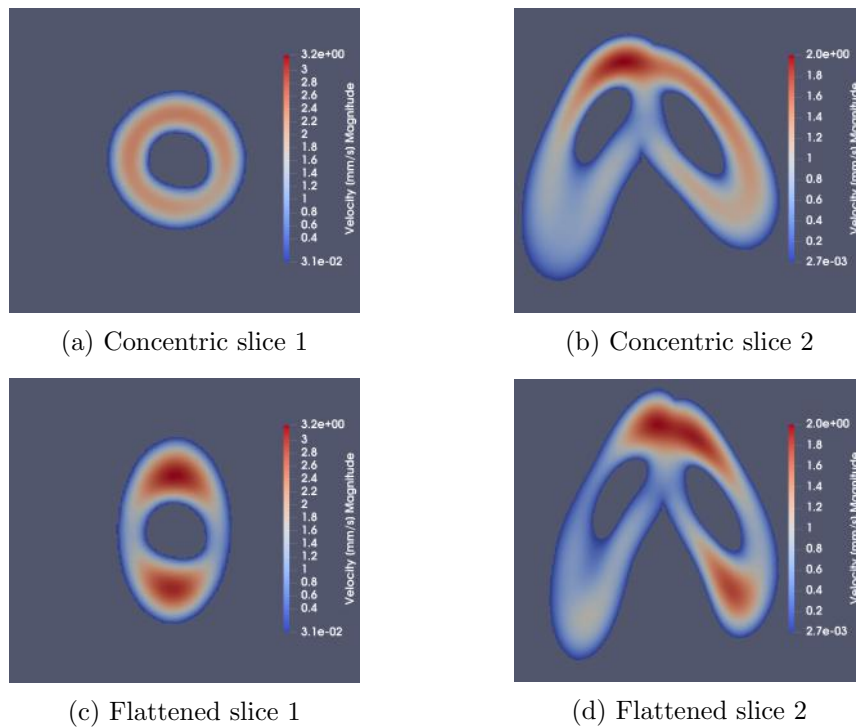


Figure 8.10: Bifurcation velocity profiles

very slow flow below the artery. In these slices it can also clearly be seen that the twisting of the flattened artery results in a difference in the velocity distribution, as the flow is more to the left side of the artery compared to the concentric case.

The last of the velocity slices, shown in figures 8.11c and 8.11f, are located after the last bend shown in figure 8.9 which is a part of the artery which bends towards the left and upwards. The results however show velocity profiles which are rather similar to those seen in straight geometries, with the effect of the bend to the left still visible in the concentric case due to the flow being dominant to the right of the artery, but an almost evenly distributed flow is seen in the flattened geometry.

In general the velocity profiles throughout the cornering section show that in the middle of the corners both geometries show a single dominant flow area as can be seen in figures 8.11b and 8.11e, however these effects are diminished real quick after the corners as seen in the last set of slices. The shape of the flattened geometry does determine the distribution of the flow, as it can be seen that due to the twisting of the flattened geometry the flow is pushed in to regions where it is not expected based on the cornering.

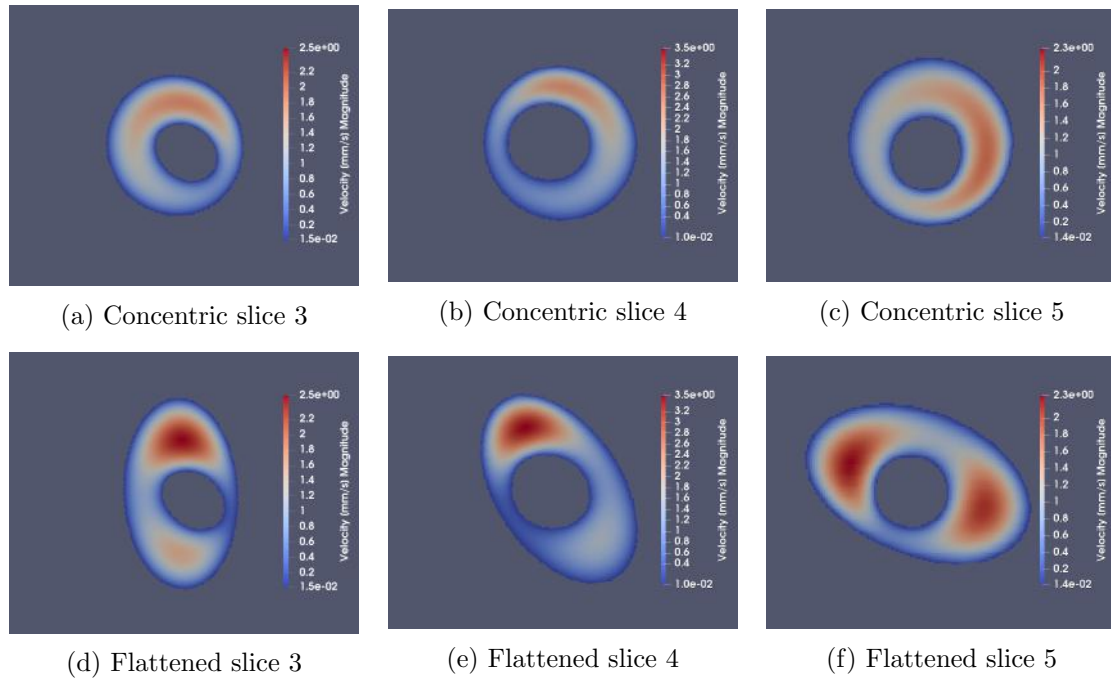


Figure 8.11: Velocity profile slices in the right cornering section

### 8.3.2 Streamline plots

The second part of the analysis contains the streamlines and the glyph plots of the bifurcation and right cornering region. In general these two types of plots show similar results, as they are used to visualise the flow. However, where the streamlines are a great tool to show the general flow in the region it is less suited for directional and temporal development of the flow. Therefore the glyph plots are used at different time steps to show the development of the flow at several critical time steps in the simulation. First the streamline plots will be discussed.

In figure 8.12 the results for the bifurcation part can be seen and in figure 8.13 the results for the right cornering section can be seen. These streamline plots are constructed by placing an evenly spaced sphere at the centre of the artery at the inlet. Within this sphere a number of points are evenly spaced and their expected path is calculated by reading the velocity data at each passing cell. In both geometries the sphere is placed at the exact same location and the same amount of streamlines are constructed such that comparable results are obtained. The streamlines are furthermore coloured based on the local velocity using the same colour bar for both geometries as is shown at the top of the figures.

First looking at the top view of the bifurcation, figure 8.12a and 8.12c, the splitting of the flow into the two arteries is clearly visible. It should be noticed that in both geometries a disturbance of the flow can be seen in the streamlines flowing into the left artery, this is caused due to a sudden expansion of the inner artery diameter which is present in the geometry and therefore expected. In general an expected result is seen where the flow in the concentric geometry is evenly distributed compared to a more dominant flow in the centre for the flattened geometry. It can also be seen that in both cases the highest velocity flow enters the right artery, however this is more present in the flattened case compared to the concentric case, which is in agreement with the velocity profiles discussed in section 8.3.1. Directly after the bifurcation a void region is shown for both geometries where almost no

flow is present. In figures 8.12b and 8.12d the side views are shown. In these plots the streamlines going into the left artery have been removed from the figure to obtain a more clear view of the flow entering the right artery. This side view shows clearly the difference in distribution of the flow, whereas once again in the concentric case the flow is distributed around the entire artery and in the flattened case two distinct flows can be seen.

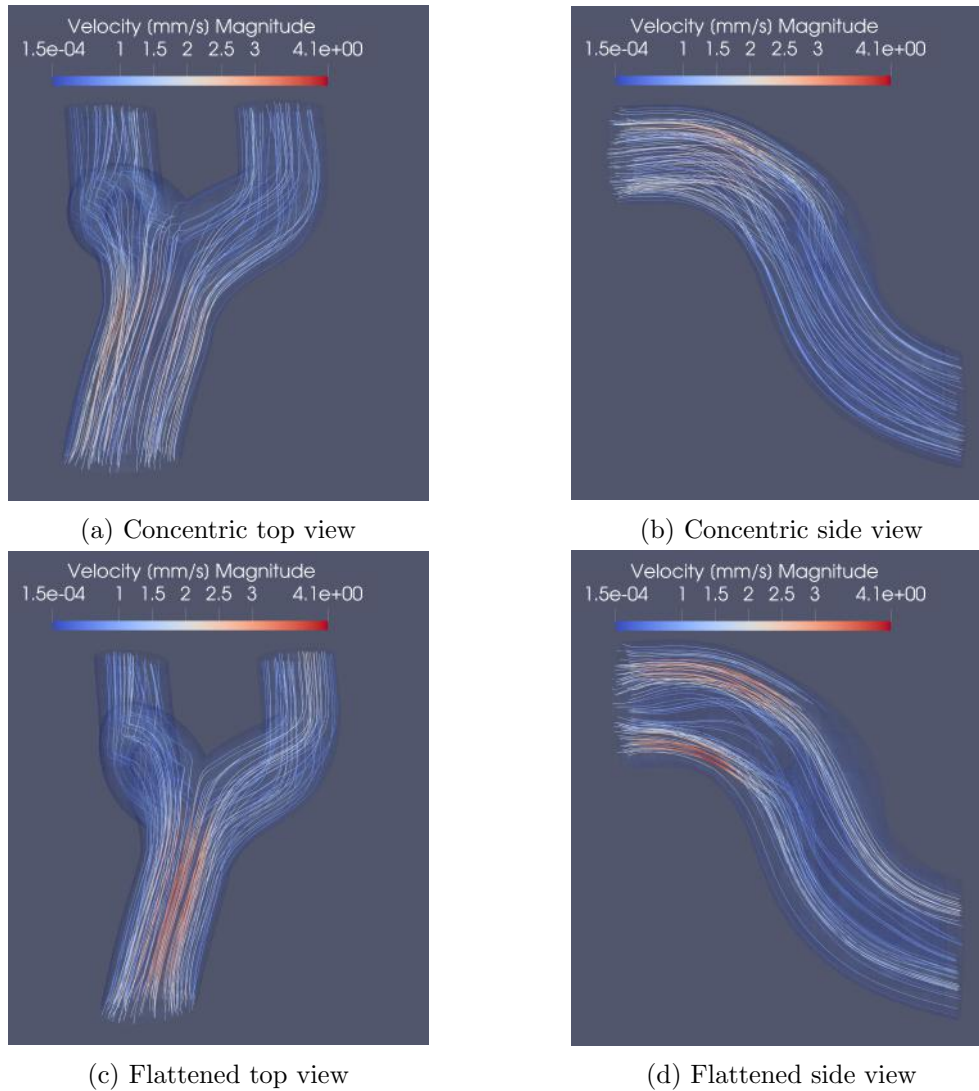


Figure 8.12: Bifurcation streamlines

The streamlines of the right cornering section are shown both viewed from the back, figures 8.13a and 8.13c, and from the top, figures 8.13b and 8.13d. In the plots shown from the back it can clearly be seen that the highest velocity flow is present above the artery, which confirms the observations made in section 8.3.1. Furthermore the flow follows roughly the same path except for the end of the cornering section, where due to the twisting of the flattened geometry the flow is directed differently than the natural flow of the concentric case. When comparing the local velocities in the cornering section it can be seen that the flow reaches velocities about 1.6 times as fast in the flattened case compared to the concentric case. This is higher than observed in chapter 6, however due to the fact that the artery is not exactly centred throughout the geometry it is expected to observe values somewhere between the flattened and off-centered case.

In the top view, figures 8.13b and 8.13d, the expected distinction between the concentric and flattened case can be seen as in the latter part of the geometry the streamlines for the concentric case are evenly distributed around the arteries whereas in the flattened case they are clustered in the two main lobes of the geometry being left and right of the artery in this case. Furthermore it can be seen that in the flattened case almost no flow is present in the tight gaps of the geometry and there is almost no crossover between the two flow channels in the cornering section.

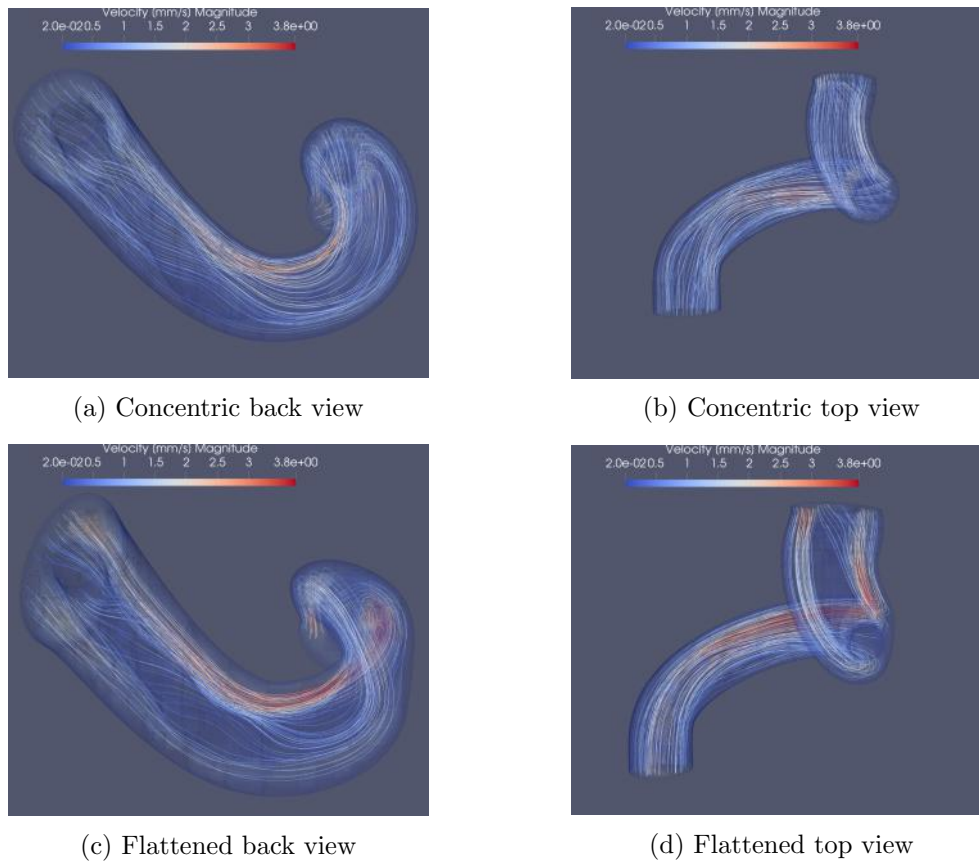


Figure 8.13: Streamlines in the right cornering section

So in summary it can be said that looking at the streamlines a clear laminar flow pattern is seen for the concentric geometry where the flow is distributed rather equally around the artery expect for the tight corners. Whereas in the flattened geometry case a clear separation between two flow streams can be seen with little to no crossover between the two. Furthermore due to the geometry of the flattened case in trying to keep the elliptical cross-section normal to the artery more twisting in the flow can be seen and thus more complex streamlines.

### 8.3.3 Glyph plots

To be able to analyse the temporal development of the flow several visualisations of the flow have been made at different time steps. The analysis is once again focused on the bifurcation region in the beginning of the geometry and the right cornering section after that. To be able to see the difference between the different stages of the flow in the geometry the flow is visualised at 4 time steps which are indicated below and shown in figure 8.14 with respect to the inlet velocity profile. These time steps are selected as they show the most significant flow in both upwards and downwards direction as well as the flow behaviour slightly after the directional changes. In figure 8.15 and 8.16 the visualisations of the flows in the bifurcation are shown for respectively the concentric and the flattened geometry and in figure 8.17 and 8.18 the visualisations of the flows in the right cornering section are shown for respectively the concentric and the flattened geometry.

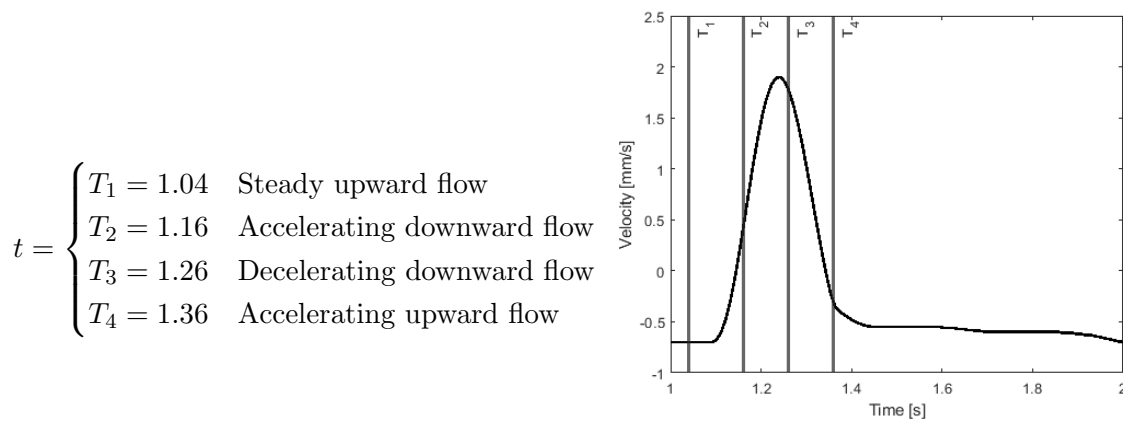


Figure 8.14: Time steps for glyph plots

First the comparison between the bifurcation section of both geometries will be done. As this is the first part of the geometry after the inlet this section is still heavily and directly influenced by the inlet velocity condition. It is therefore very clearly visible what the different time steps are visualising. Looking at figure 8.15a a steady negative flow towards the inlet of the geometry is visible, with the highest velocities being present before the bifurcation, which is to be expected as the total flow is split over the two arteries afterwards. In figure 8.15b the direction of the flow has just changed, showing a velocity flow going into the geometry however not much flow is yet present in the arteries as the velocity at the inlet is low and the time passed is little. In figure 8.15c the maximum velocity of the flow has just been passed and the flow just started decelerating, it is clearly visible that a concentric geometry is used here as the flow is present around the entire artery and evenly distributed. Compared to the previous time step it shows a lot more flow into the geometry. In figure 8.15d the flow once again just changed directions, this time going into an upward flow, once again the entire geometry follows this direction of flow, with very little velocity being present at the end of the bifurcation.

Comparing this bifurcation section to the flattened geometry results shown in figure 8.16 a few things should be mentioned. First of all the expected distribution of the flow into two main channels is visible in figure 8.16a and 8.16c, where it should also be noted that after the bifurcation the two distinct flows reduce a bit and a more evenly distributed flow is visible. In both cases just after changing the direction of flow the distinct two flows can be seen before the bifurcation, however after the bifurcation almost no flow is present and the

expected distribution is not quite noticeable. Both geometries show similar results at the chosen time steps, which can be explained as this bifurcation is closely located to the inlet.

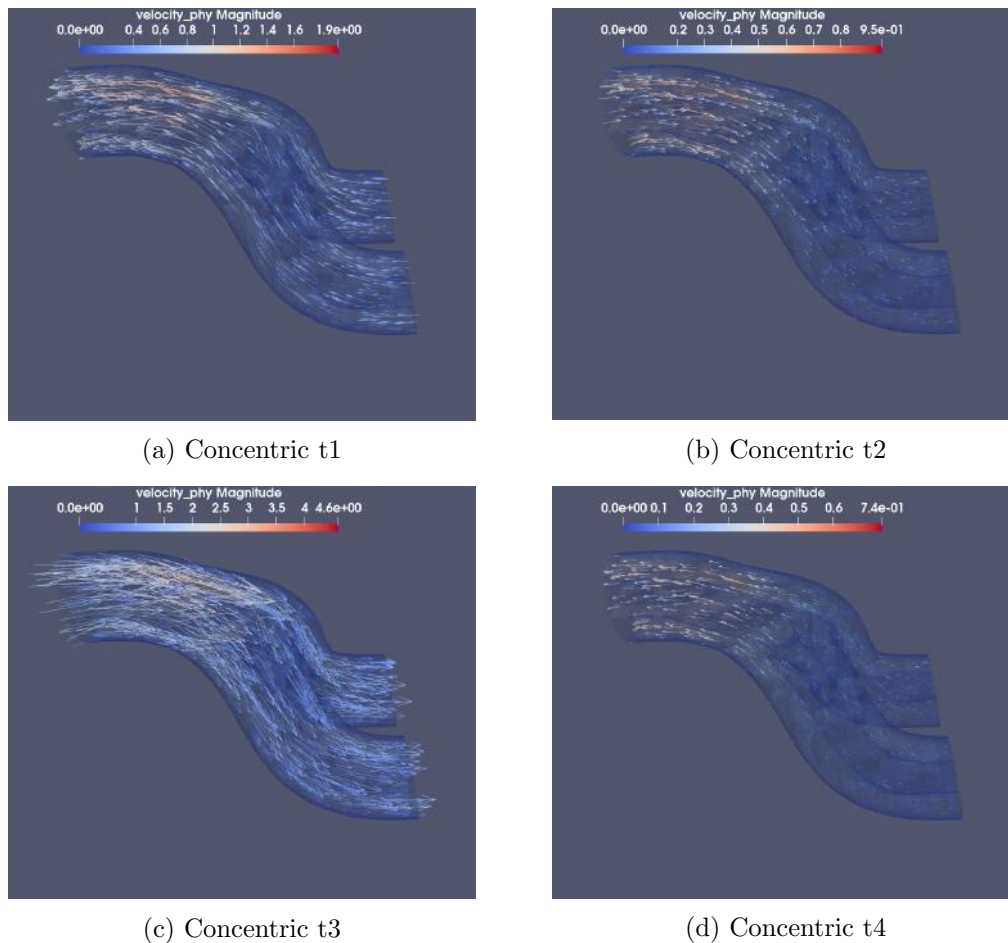


Figure 8.15: Flow visualisation in the concentric bifurcation section

In the glyph plots of the cornering section in figures 8.17 and 8.18 it should be stated first that the geometry inlet is located at the right and the outlet is towards the left. Therefore downward (positive) flow is from right to left and upward (negative) flow is from left to right.

First of all evaluating the concentric case. In figure 8.17a the steady upward flow is present, which in the cornering section shows a clear dominant flow in the inner corners and a slower flow at the outer corners. The flow however is evenly across the entire geometry, showing similar magnitudes of flow velocity at the beginning and end of the geometry. In figure 8.17b the flow has just changed direction, which is clearly visible in this visualisation. At the beginning of the geometry a downward flow is visible, still being rather low velocity. In the middle of the cornering no flow is present due to the collision of the two directional flows, as at the end of the geometry still an upward flow can be seen. In figure 8.18c a steady downward flow is visible where the flow shows the same behaviour as seen at the first time step, but in reverse direction. In figure 8.18d the direction of the flow has once again changed, however in this case it is already more developed than in figure 8.18b, as at the beginning of the geometry and in the first corner a clear upward flow is visible, but at the end of the geometry almost no flow is yet present as this part is still changing flow directions.

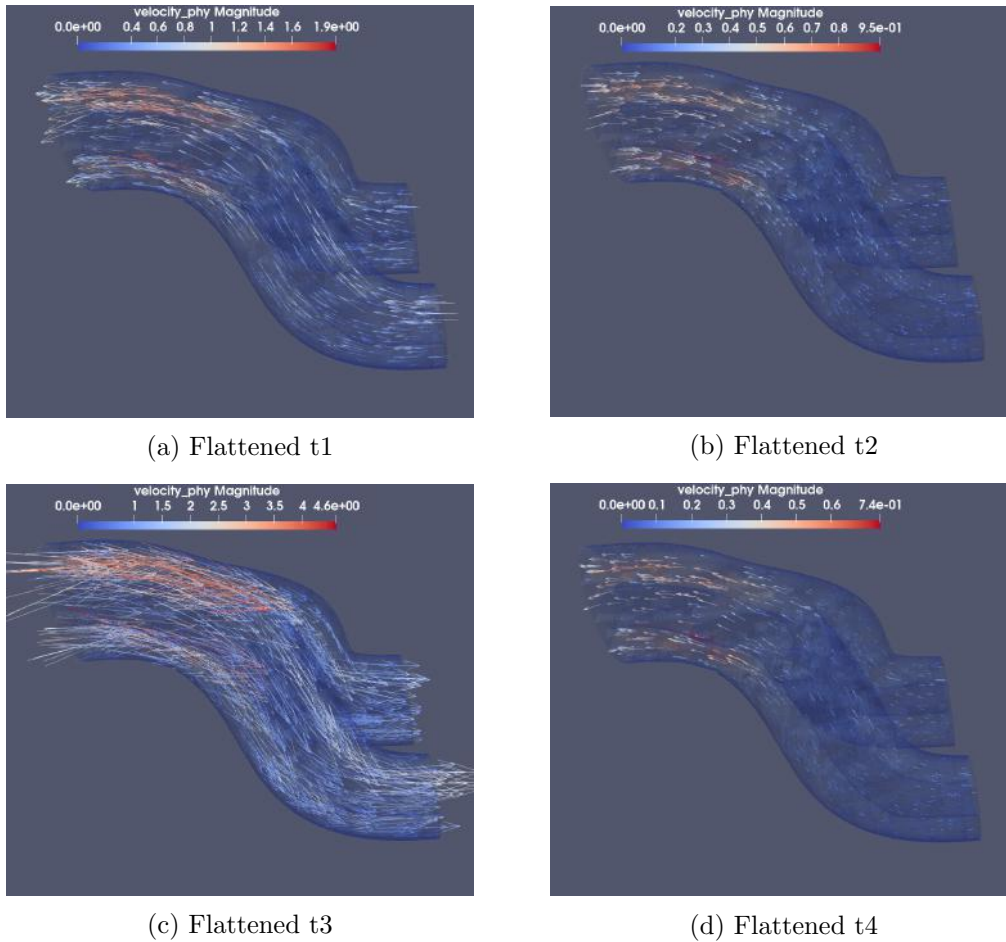


Figure 8.16: Flow visualisation in the flattened bifurcation section

Evaluating the right cornering section in the flattened geometry shows interesting results. First of all taking a look at figure 8.18a a similar flow pattern to the concentric case can be seen. In the concentric case the flow is a bit more on top of the artery, which is the same observation as was made in the velocity profile analysis. However, it can clearly be seen that both flows attempt to follow the same path, but this is limited due to the twisting of the flattened geometry. In figure 8.18b the same collision of flow directions is visible as in the concentric geometry. A downward flow is visible in the beginning of the geometry, almost no flow in the cornering and then a little upward flow at the end of the geometry. In figure 8.18c the distinction between the two geometries is once again more visible. Even though both geometries have the bulk flow following almost the same route, the concentric geometries shows a more evenly distributed flow in the beginning and end of the geometry, whereas the flattened case clearly shows two distinct flow channels. In figure 8.18d a similar flow is seen as in the concentric case at this time step, however it is less developed yet. The flow has just changed direction and is clearly present in the beginning of the geometry, however in the cornering and at the end of the geometry no flow has yet been established, whereas in the concentric case the flow in the cornering had already been established. The differences between the geometries in the development of the flow at these time steps is to be expected as the local velocities are significantly different and in these plots, just after the changing of flow direction at time steps  $T_2$  and  $T_3$ , the bulk flow is most visible.

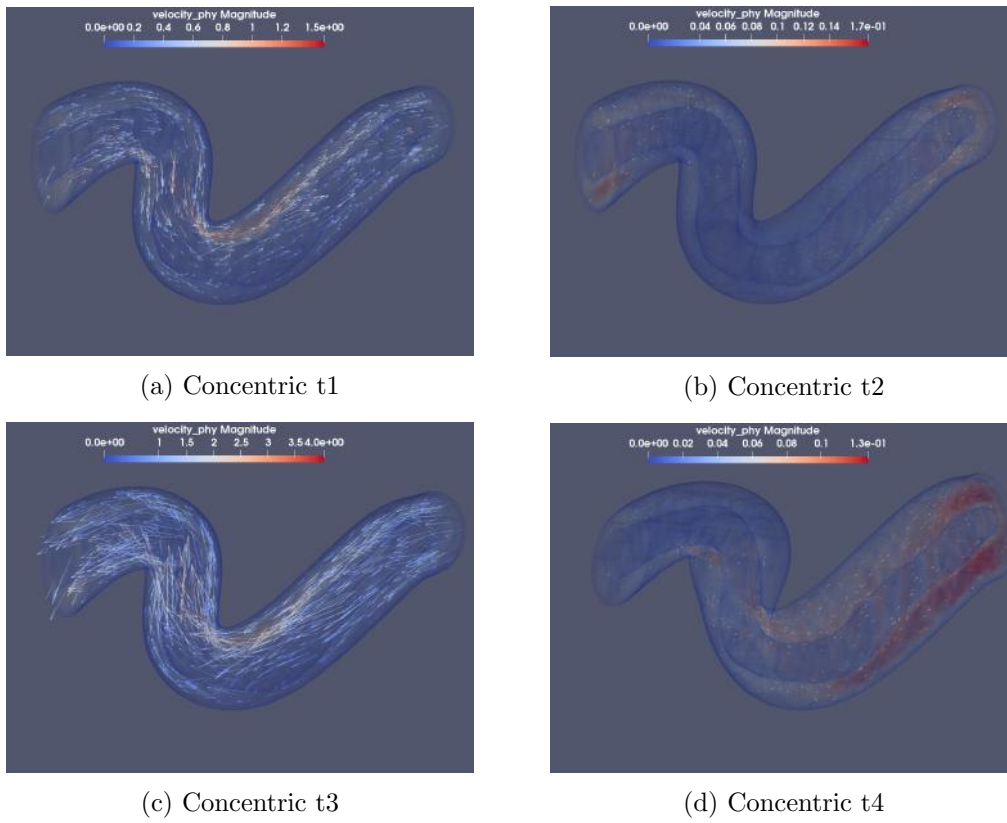


Figure 8.17: Flow visualisation in the concentric right cornering section

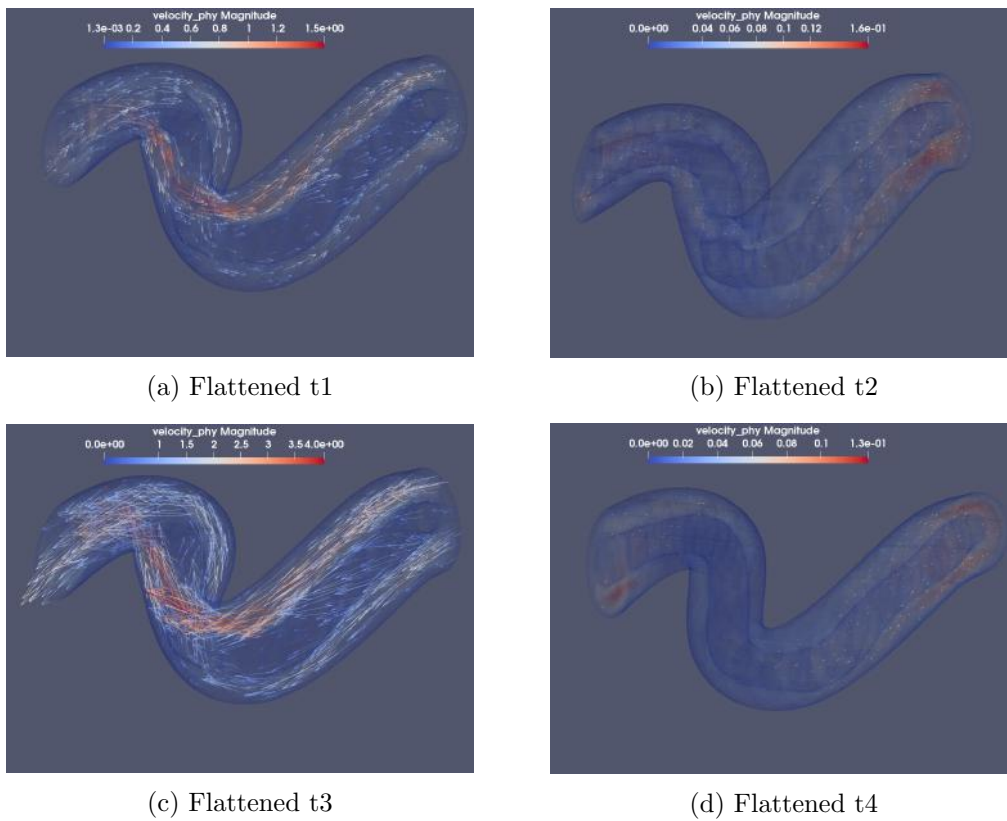


Figure 8.18: Flow visualisation in the flattened right cornering section

### 8.3.4 Velocity profiles over time

To evaluate the temporal development of the flow a total of 9 points have been taken within the geometry over which the velocity is analysed over time. These 9 points are distributed such that there is 1 shared point before the bifurcation and then another 4 points distributed over the length of each of the bifurcated arteries. The exact node is in general selected straight above the artery, however due to the twisting of the flattened geometry in several location there is almost no flow straight above the artery. Therefore, the node with the maximum velocity is selected in the flattened geometry, after which this location is transposed to the concentric geometry for the concentric analysis node. In figure 8.19 the locations of these points are shown in the mesh of the concentric geometry and in table 8.4 the coordinates of the different points are stated. To be able to completely analyse the flow, both the magnitude of the velocity is recorded as well as the individual components of the velocity.

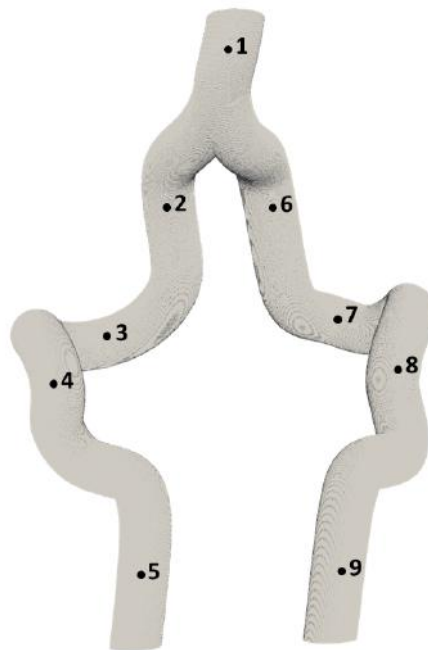


Figure 8.19: Indicated location of analysis points

Table 8.4: Coordinates of velocity analysis points

	Concentric PVS shape			Flattened PVS shape		
	X [mm]	Y [mm]	Z [mm]	X [mm]	Y [mm]	Z [mm]
Point 1	3.6	4.23	1	3.58	4.27	1
Point 2	2.63	2.32	3	2.61	2.35	3
Point 3	1.5	0.84	4.68	1.13	0.99	4.78
Point 4	1.11	1.63	6	1.15	1.63	6
Point 5	2.04	1.66	8.4	2.02	1.74	8.4
Point 6	4.35	2.17	3	4.31	2.22	3
Point 7	5.4	0.26	4.1	5.4	0.14	4.13
Point 8	5.95	1.7	6	5.9	1.76	6
Point 9	5.23	1.9	8.4	5.21	1.94	8.4

In figure 8.20 the different velocity plots are shown for the shared point 1 and the points 2 to 5 located in the left artery. Here plots (a) till (d) are showing the results of the concentric geometry and plots (e) till (h) show the results of the flattened geometry. It should be noted that the y-axis in the plots do not show the same range of values, this is chosen such that the shape of the curves can be compared more easily, whereas the difference in magnitude of the flow is already discussed in the previous simulations and analysis.

In general it can be seen that the magnitude of the velocity is lower for points further down in to the PVS, which is to be expected, with the exception of point 2. This is only explainable due to this point being located right after the bifurcation, where due to the larger shape of the joined PVS of both bifurcated arteries the CSF flowed through a larger region which resulted in a velocity loss.

Furthermore the plots are showing very similar results, varying very little between the concentric and flattened case except for some small magnitude differences between the different points. The main difference is seen in the vertical velocity (or Y-velocity) in point 4. In the concentric case the vertical velocity achieves only small negative values in point 4, thus implicating a downward stream which is to be expected in this part of the geometry. In the flattened case the vertical velocity in point 4 reaches a positive value, thus indicating an upward stream. This can be explained due to the fact that the flattened geometry in this cornering section twists from a vertical elliptical shape to a horizontal elliptical shape, thus pushing the fluid below the artery upwards and the fluid above the artery downwards.

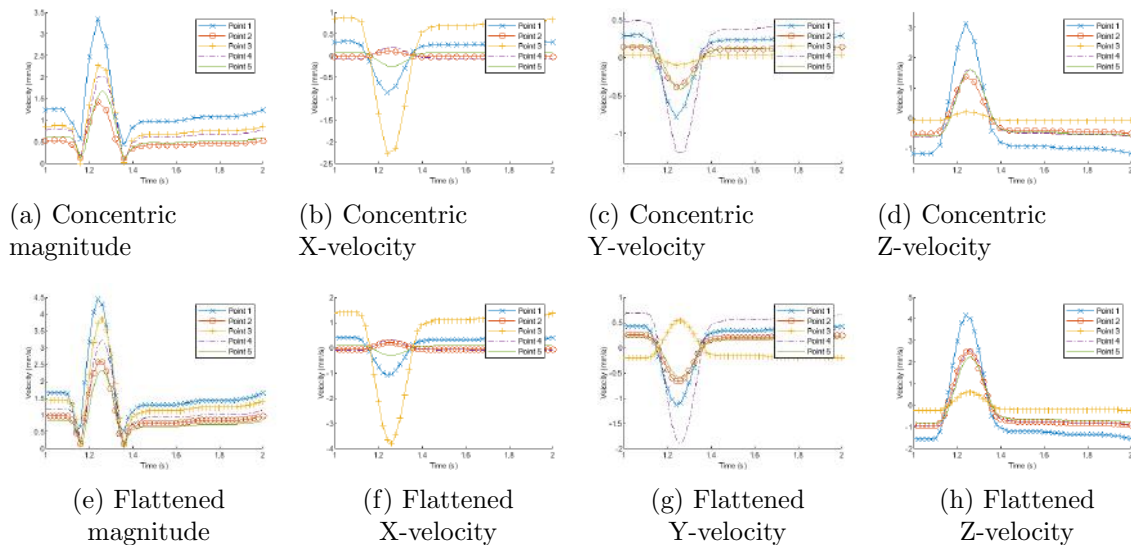


Figure 8.20: Velocity over time data for left artery

In figure 8.21 the resulting plots of the 5 points in the right artery are shown, where point 1 is once again the shared point before the bifurcation. The results are very similar with regards to the left artery. This similarity is to be expected due to the locations being roughly equal, but this also confirms the assumption made in the previous analysis where the symmetry of the geometry is used to focus on the bifurcation and right cornering section. Once again the differences between the concentric and flattened case are apart from the magnitude differences minimal, however some interesting things should be noted.

In point 6, right after the bifurcation, once more a relatively low velocity magnitude is seen with respect to the other points, which indicates once again that right after the bifurcation a velocity loss is present. The main differences in the shape of the velocity curves in this side of the geometry is again seen in the vertical velocity. In both point 7 and point 8 differences between the concentric and flattened geometries are noted. In point 7 the vertical velocity increases in the flattened case whereas in point 8 the vertical velocity decreases relative to the other points. This is once again the result of the twisting of the cross-section of the geometry, which pushes the flow more upwards or downwards depending on the direction of the corner and the twist.

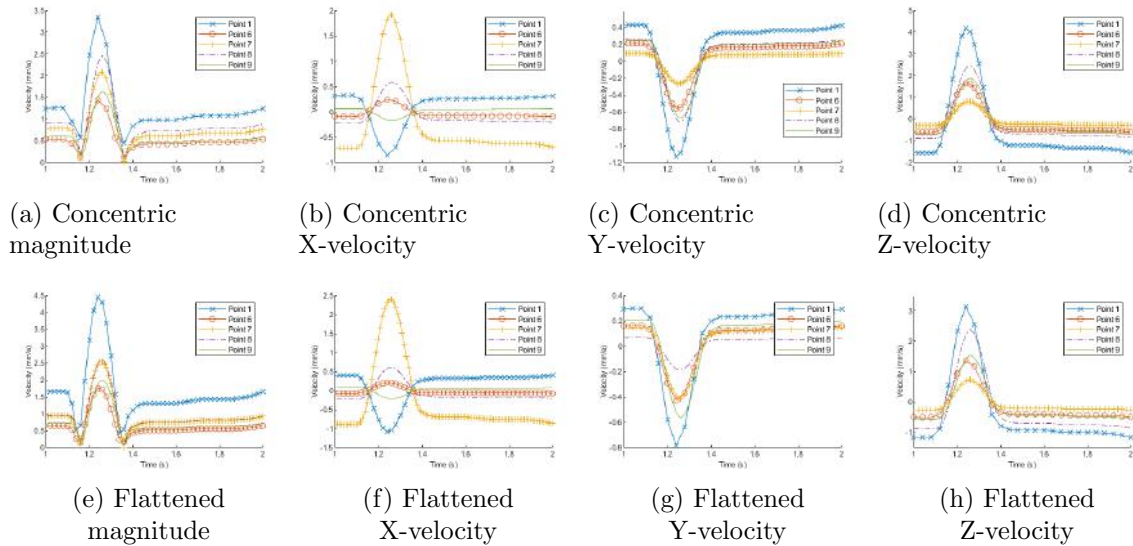


Figure 8.21: Velocity over time data for right artery

## Chapter 9

# Discussion, conclusions and recommendations

In this chapter the report will be finalised. First the obtained results and several noteworthy choices made will be discussed. Then the research questions stated in the introduction will be answered and the conclusions of this thesis are stated. Finally recommendations for further research will be made, what is the next step in this line of research and how could this research be improved upon.

### 9.1 Discussion

In this section first the setup of the simulations will be discussed, after which the results of the different sets of simulations will be discussed.

All the simulations done in this thesis have used the measurement of the CSF flow in the PVS of mice. These measurement have been performed by multiple researchers [27][29][31], such that these results can be assumed to be valid for their specific cases. However, there are two uncertainties regarding the use of these measurements in this thesis that need to be discussed. First of all to what extent do the microsphere measurements equal the CSF velocity flow and secondly whether the conversion to the human brain scale is accurately enough.

The measurements of the CSF flow in PVS in mice are done by image tracking of microspheres injected in the CSF flow. The movement of the microspheres is then assumed to be equal to the CSF flow, however these microspheres do have a mass and size and might therefore deviate slightly from the CSF flow. In the results presented in chapter 7 this was already briefly discussed, as it is to be expected that these microspheres will follow the bulk flow of the CSF and are more likely to get stuck in the slower flowing and narrower regions around the artery. The researchers mentioned in their respective papers that particles that got stuck were eliminated from the measurements, however as long as a slight movement was present they were accounted for. This uncertainty could result in both a faster or a slower actual CSF flow in the PVS. It could be that the CSF velocity is higher than the measured values, due to microspheres that are almost stuck being taken into account in the measurements, or the average CSF flow in the PVS is slower than the measured values as all the microspheres measured were located in the regions with the highest local velocity. This uncertainty is not expected to influence the results significantly, as this will affect all the simulation studies performed in this thesis for a same amount, therefore the relative comparisons are still valid. However, when comparing this thesis with studies using new measurement in the future it

has to be taken into account.

In the simulations performed in chapter 6 and 8 the CSF flow measurements done in the mice brain were scaled to the human brain. To be able to scale these measurements, data of CSF production rates, CSF flow rates and sizes of the cerebral aqueduct in the human and mice brain were used. In the CSF flow through the cerebral aqueduct in mice it was assumed that all the produced CSF in the brain would move through the cerebral aqueduct. This is a very rough estimate as most likely the fluid will partially exit the ventricles through other channels and porous walls as well. Therefore the CSF flow in PVS of humans as used in chapter 6 and 8 should be seen as a very rough estimate. More research on the CSF flow in the human brain should be done to be able to accurately define the CSF velocity flow in the PVS. Also, more research of the CSF flow in mice could be done to be able to accurately use a conversion method as suggested in this thesis. The conversion method used in this thesis will result in CSF flow velocities in the PVS of the same order of magnitude as is to be expected in the real brain, however it is a rough estimate. This discrepancy once again is not expected to significantly alter the results presented in this thesis as it will merely result in a quantitative difference, but this is off the same effect for each of the three geometries used in this thesis. Therefore, the results with respect to the other geometries used here will stay the same.

In the geometries used in the different simulation studies several simplification were made to the artery and the PVS. First of all the walls were assumed to be rigid. This assumption is very common in simulation studies and will alter the results slightly as artery walls should have an elastic component. However, this won't be expected to influence the results significantly.

The walls were also assumed to be static. Most researches that have currently been performed on the driving forces of CSF flow have mentioned arterial wall pulsations as one of the main driving forces of either the bulk flow or the oscillatory component of the flow [30]. It was mentioned in chapter 7 that this thesis is focused on how the fluid moves and not why the fluid moves. However, it should be noted that arterial wall pulsations will quite significantly affect how the fluid moves. Recently research has been performed on peristaltic pumping in flattened geometries [63]. These wall movements induce much more three-dimensional movement to the flow, which causes a lot more disturbance in the flow. This effect is increased with increased eccentricity, therefore the effects are expected to be even more significant for an off-centered artery. In the simulations performed in this thesis the walls were assumed to be static and it was shown that the effect of the cross-sectional shape has to be taken into account for further simulation studies. The results obtained by this new study therefore amplifies the need for more research on this subject as the differences are expected to be much more significant.

The results obtained in chapter 8 have shown that the cross-sectional shape of the PVS influences the distribution of the flow around the artery. However, much of these changes between the flows are related to the twisting of the flattened PVS shape. This twisting had to be included in the geometry used in this thesis to be able to follow the tight corners without having the PVS intersect itself. Whether this twisting of the PVS is a realistic behaviour is unknown, currently only MRI images of cross-sectional shapes of the PVS are known in straight arteries. It is interesting to investigate how the PVS is shaped around an artery with a tight bend.

## 9.2 Conclusions

In order to draw the conclusions of this thesis first the research question and its sub questions are recalled:

**”To what extent does the cross-sectional shape of the PVS influence the fluid behaviour of CSF?”**

1. What are valid cross-sectional shapes for the perivascular space?
2. What simplifications of the geometry are valid to make in this case?
3. To what extent are previously performed simulation studies using concentric PVS shapes still valid?

In this thesis three different cross-sectional shapes have been used for the simulations, being a concentric annulus, a flattened annulus and a flattened annulus with an off-centered artery. These geometries are based on MRI images of the PVS in the brains of mice and human.

Simplifications are made to the geometry of the PVS as the walls are assumed to be rigid and static. In a real case the the artery wall will have an elastic component and pulsatile movement, however this would have complicated the simulation significantly.

It has been shown in the different simulation studies that previously performed research using a concentric PVS shape still have value. It should be noted that the local velocities and the flow distribution around the artery change significantly. However, the flow doesn't leave the laminar region in either geometry, the magnitude differences are smaller around bifurcations, and the flow distribution shows more similarities in the corner sections. Therefore, previously performed simulations using a concentric PVS could still provide useful insights, but for future research a more realistic PVS shape should be used.

To answer the main research question of this thesis three different simulation studies have been performed. It has been shown that the local velocity can increase by up to 150% when comparing the flattened to the concentric geometry and up to 190% when the artery is off-centered. Also, the flow distribution around the artery is changed significantly with the cross-sectional shape, shifting from an evenly distributed flow in the concentric shape to a flow with two dominant regions in the flattened shape and a single dominant flow region in the off-centered shape. The local velocity differences have been shown to reduce around a bifurcation, where a more similar flow distribution is seen between the concentric and the flattened shape. In the cornering regions both flows show a single dominant flow region, however the flow in the flattened geometry is forced to a different path due to the twisting of its geometry.

### 9.3 Recommendations

For future research several improvements to this thesis are proposed as well as new research with respect to this topic.

To improve on the knowledge of this topic more MRI studies should be performed on the PVS, currently only MRI images are available of PVS shapes around slices of a straight artery. However, it has been shown that the PVS can be a discontinued annulus, this occurs when the PVS is flattened to such a degree that the artery is larger in diameter than the width of the PVS, but it should be investigated how often this occurs and how this shape develops over the length of the artery. Furthermore, the shape of the PVS around a bifurcating artery and a tight cornering section of an artery should be determined such that more accurate geometries can be made.

The main improvement to this research is the addition of a pulsatile arterial wall to the simulations. The addition of a pulsatile wall will influence the streamlines of the flow significantly as it will induce more three-dimensional disturbance. Furthermore, the effect of these wall displacement on the magnitude of the flow is of interest. Recently research has been done on this perivascular wall pumping in eccentric pipes, but those geometries have only been similar to the straight arteries used in the first two simulations in this thesis. It would be interesting to investigate the results of this addition on a more complex geometry like the realistic artery with PVS used in this study.

Adding the pulsatile wall movement is also a part of implementing the driving forces of CSF in the PVS. In this thesis an inlet velocity profile has been used which was a resultant of several driving forces, but when implementing the driving forces to the simulation the results might differ from this study.

# Bibliography

- [1] “World Health Organization - Dementia.” [Online]. Available: <https://www.who.int/news-room/fact-sheets/detail/dementia>
- [2] Mayo Clinic, “Alzheimer’s disease - symptoms and causes.” [Online]. Available: <https://www.mayoclinic.org/diseases-conditions/alzheimers-disease/symptoms-cause/s/syc-20350447>
- [3] W. Wong, “Economic burden of alzheimer disease and managed care considerations,” *The American Journal of Managed Care*, vol. 26, pp. S177–S183, 8 2020.
- [4] J. M. Tarasoff-Conway, R. O. Carare, R. S. Osorio, L. Glodzik, T. Butler, E. Fieremans, L. Axel, H. Rusinek, C. Nicholson, B. V. Zlokovic, B. Frangione, K. Blennow, J. Ménard, H. Zetterberg, T. Wisniewski, and M. J. de Leon, “Clearance systems in the brain—implications for alzheimer disease,” *Nature Reviews Neurology*, vol. 11, pp. 457–470, 8 2015.
- [5] J. H. Thomas, “Fluid dynamics of cerebrospinal fluid flow in perivascular spaces,” *Journal of the Royal Society Interface*, vol. 16, no. 159, 2019.
- [6] M. E. Watts, R. Pocock, and C. Claudianos, “Brain energy and oxygen metabolism: Emerging role in normal function and disease,” *Frontiers in Molecular Neuroscience*, vol. 11, 6 2018.
- [7] B.-L. Sun, L. hua Wang, T. Yang, J. yi Sun, L. lei Mao, M. feng Yang, H. Yuan, R. A. Colvin, and X. yi Yang, “Lymphatic drainage system of the brain: A novel target for intervention of neurological diseases,” *Progress in Neurobiology*, vol. 163-164, pp. 118–143, 4 2018.
- [8] S. B. Hladky and M. A. Barrand, “Elimination of substances from the brain parenchyma: efflux via perivascular pathways and via the blood–brain barrier,” *Fluids and Barriers of the CNS*, vol. 15, p. 30, 12 2018.
- [9] L. Sakka, G. Coll, and J. Chazal, “Anatomy and physiology of cerebrospinal fluid,” *European Annals of Otorhinolaryngology, Head and Neck Diseases*, vol. 128, no. 6, pp. 309–316, 2011.
- [10] “Subarachnoid space: Structure and function — kenhub.” [Online]. Available: <https://www.kenhub.com/en/library/anatomy/subarachnoid-space>
- [11] L. N. Telano and S. Baker, “Physiology, cerebral spinal fluid,” *StatPearls*, 7 2021. [Online]. Available: <https://www.ncbi.nlm.nih.gov/books/NBK519007/>
- [12] R. D. Terlizzi and S. Platt, “The function, composition and analysis of cerebrospinal fluid in companion animals: Part i - function and composition,” *Veterinary Journal*, vol. 172, pp. 422–431, 11 2006.

- [13] P. Wostyn, D. Van Dam, K. Audenaert, H. E. Killer, P. P. De Deyn, and V. De Groot, "A new glaucoma hypothesis: A role of glymphatic system dysfunction," *Fluids and Barriers of the CNS*, vol. 12, no. 1, pp. 1–6, 2015.
- [14] A. de Lahunta and E. Glass, "Cerebrospinal fluid and hydrocephalus," *Veterinary Neuroanatomy and Clinical Neurology*, pp. 54–76, 2009.
- [15] N. A. Jessen, A. S. F. Munk, I. Lundgaard, and M. Nedergaard, "The Glymphatic System: A Beginner's Guide," *Neurochemical Research*, vol. 40, no. 12, pp. 2583–2599, 2015.
- [16] B. L. Wright, J. T. Lai, and A. J. Sinclair, "Cerebrospinal fluid and lumbar puncture: A practical review," *Journal of Neurology*, vol. 259, no. 8, pp. 1530–1545, 2012.
- [17] "Ventricular system of the brain." [Online]. Available: <https://www.thoughtco.com/ventricular-system-of-the-brain-3901496>
- [18] B. IG, J. IH, and B. LE, "Effects of proteins, blood cells and glucose on the viscosity of cerebrospinal fluid," *Pediatric neurosurgery*, vol. 28, no. 5, pp. 246–251, 1998. [Online]. Available: <https://pubmed.ncbi.nlm.nih.gov/9732257/>
- [19] J. J. Iliff, M. Wang, Y. Liao, B. A. Plogg, W. Peng, G. A. Gundersen, H. Benveniste, G. E. Vates, R. Deane, S. A. Goldman, E. A. Nagelhus, and M. Nedergaard, "A paravascular pathway facilitates csf flow through the brain parenchyma and the clearance of interstitial solutes, including amyloid beta." *Science translational medicine*, vol. 4, p. 147ra111, 8 2012.
- [20] M. L. Rennels, T. F. Gregory, O. R. Blaumanis, K. Fujimoto, and P. A. Grady, "Evidence for a 'paravascular' fluid circulation in the mammalian central nervous system, provided by the rapid distribution of tracer protein throughout the brain from the subarachnoid space." *Brain research*, vol. 326, pp. 47–63, 2 1985.
- [21] J. M. Wardlaw, H. Benveniste, M. Nedergaard, B. V. Zlokovic, H. Mestre, H. Lee, F. N. Doubal, R. Brown, J. Ramirez, B. J. MacIntosh, A. Tannenbaum, L. Ballerini, R. L. Rungta, D. Boido, M. Sweeney, A. Montagne, S. Charpak, A. Joutel, K. J. Smith, and S. E. Black, "Perivascular spaces in the brain: anatomy, physiology and pathology," *Nature Reviews Neurology*, vol. 16, pp. 137–153, 3 2020.
- [22] G. Barisano, M. Law, R. M. Custer, A. W. Toga, and F. Sepehrband, "Perivascular space imaging at ultrahigh field mr imaging," *Magnetic Resonance Imaging Clinics of North America*, vol. 29, pp. 67–75, 2 2021.
- [23] S. Hetts, A. Yen, D. Cooke, J. Nelson, P. Jolival, J. Banaga, M. Amans, C. Dowd, R. Higashida, M. Lawton, H. Kim, and V. Halbach, "Pial artery supply as an anatomic risk factor for ischemic stroke in the treatment of intracranial dural arteriovenous fistulas," *American Journal of Neuroradiology*, vol. 38, no. 12, pp. 2315–2320, 2017. [Online]. Available: <http://www.ajnr.org/content/38/12/2315>
- [24] J. A. Bevan, J. Dodge, C. L. Walters, T. Wellman, and R. D. Bevan, "As human pial arteries (internal diameter 200–1000 micrometer) get smaller, their wall thickness and capacity to develop tension relative to their diameter increase," *Life Sciences*, vol. 65, pp. 1153–1161, 8 1999.
- [25] G. Mchedlishvili, D. Baramidze, and L. Nikolaishvili, "Functional behaviour of pial and cortical arteries in conditions of increased metabolic demand from the cerebral cortex," *Nature*, vol. 213, pp. 506–507, 1967.

- [26] N. Thorin-Trescases, T. Bartolotta, N. Hyman, P. L. Penar, C. L. Walters, R. D. Bevan, and J. A. Bevan, "Diameter dependence of myogenic tone of human pial arteries," *Stroke*, vol. 28, no. 12, pp. 2486–2492, 1997.
- [27] H. Mestre, J. Tithof, T. Du, W. Song, W. Peng, A. M. Sweeney, G. Olveda, J. H. Thomas, M. Nedergaard, and D. H. Kelley, "Flow of cerebrospinal fluid is driven by arterial pulsations and is reduced in hypertension," *Nature Communications*, vol. 9, no. 1, 2018.
- [28] A. J. Schain, A. Melo-Carrillo, A. M. Strassman, and R. Burstein, "Cortical spreading depression closes paravascular space and impairs glymphatic flow: Implications for migraine headache," *The Journal of Neuroscience*, vol. 37, pp. 2904–2915, 3 2017.
- [29] B. Bedussi, M. Almasian, J. de Vos, E. VanBavel, and E. N. Bakker, "Paravascular spaces at the brain surface: Low resistance pathways for cerebrospinal fluid flow," *Journal of Cerebral Blood Flow and Metabolism*, vol. 38, no. 4, pp. 719–726, 2018.
- [30] C. Daversin-Catty, V. Vinje, K.-A. Mardal, and M. E. Rognes, "The mechanisms behind perivascular fluid flow," *PLOS ONE*, vol. 15, p. e0244442, 12 2020.
- [31] A. Raghunandan, A. Ladron-De-guevara, J. Tithof, H. Mestre, T. Du, M. Nedergaard, J. H. Thomas, and D. H. Kelley, "Bulk flow of cerebrospinal fluid observed in periarterial spaces is not an artifact of injection," *eLife*, vol. 10, pp. 1–15, 2021.
- [32] J. Tithof, D. H. Kelley, H. Mestre, M. Nedergaard, and J. H. Thomas, "Hydraulic resistance of periarterial spaces in the brain," *Fluids and Barriers of the CNS*, vol. 16, no. 1, pp. 1–13, 2019.
- [33] R. T. Kedarasetti, P. J. Drew, and F. Costanzo, "Arterial pulsations drive oscillatory flow of csf but not directional pumping," *Scientific Reports*, vol. 10, 12 2020.
- [34] L. Cova and M.-T. Armentero, *1980-2011: Parkinson's Disease and Advance in Stem Cell Research*, 11 2011.
- [35] R. D. Hodge, T. E. Bakken, J. A. Miller *et al.*, "Conserved cell types with divergent features in human versus mouse cortex," *Nature*, vol. 573, pp. 61–68, 9 2019.
- [36] D. Raabe, "Overview of the lattice Boltzmann method for nano- And microscale fluid dynamics in materials science and engineering," *Modelling and Simulation in Materials Science and Engineering*, vol. 12, no. 6, 2004.
- [37] M. C. Sukop and J. Daniel T. Thorne, *Lattice Boltzmann Modeling, An Introduction for Geoscientists and Engineers*. Miami, FL: Springer, 2005.
- [38] Timm Krüger *et al*, "The lattice boltzmann method principles and practice." [Online]. Available: <http://www.springer.com/series/8431>
- [39] P. L. Bhatnagar, E. P. Gross, and M. Krook, "A model for collision processes in gases. i. small amplitude processes in charged and neutral one-component systems," *Phys. Rev.*, vol. 94, pp. 511–525, May 1954. [Online]. Available: <https://link.aps.org/doi/10.1103/PhysRev.94.511>
- [40] X. He and L.-S. Luo, "Theory of the lattice boltzmann method: From the boltzmann equation to the lattice boltzmann equation," *Phys. Rev. E*, vol. 56, pp. 6811–6817, Dec 1997. [Online]. Available: <https://link.aps.org/doi/10.1103/PhysRevE.56.6811>

- [41] P. Young, “Physics 112 maxwell distributions for the speed and velocity of molecules in a gas (kittel and kroemer, p. 392-3).” [Online]. Available: <https://young.physics.ucsc.edu/112/maxwell.pdf>
- [42] H. S. An, *An introduction to the theory of the Boltzmann equation*. New York: Holt, Rienhart and Winston, Inc., 1971.
- [43] H. Liu, J. G. Zhou, and R. Burrows, “Inlet and outlet boundary conditions for the lattice-boltzmann modelling of shallow water flows,” *Progress in Computational Fluid Dynamics*, vol. 12, pp. 11–18, 2012.
- [44] Q. Zou and X. He, “On pressure and velocity boundary conditions for the lattice boltzmann bgk model,” *Physics of Fluids*, vol. 9, pp. 1591–1596, 1997.
- [45] H. Klimach, K. Jain, and S. Roller, “End-to-end parallel simulations with apes,” *Advances in Parallel Computing*, vol. 25, pp. 703–711, 9 2014.
- [46] J. Qi, K. Jain, H. Klimach, and S. Roller, “Performance evaluation of the lbm solver musubi on various hpc architectures,” in *Parallel Computing*, ser. Advances in Parallel Computing, F. Peters, M. Parsons, M. Sawyer, H. Leather, and G. Joubert, Eds. Elsevier, Jan. 2016, pp. 807–816.
- [47] “Adaptable poly-engineering simulator (APES).” [Online]. Available: <https://apes.osdn.io/>
- [48] R. Vinuesa, E. Bartrons, D. Chiu, J.-D. Rüedi, P. Schlatter, A. Obabko, and H. Nagib, *On Minimum Aspect Ratio for Experimental Duct Flow Facilities*, 08 2016, pp. 201–211.
- [49] I. Erhunmwum and M. Oladeinde, “Analysis of flow in a concentric annulus using finite element method,” *Nigerian Journal of Technology*, vol. 35, p. 344, 4 2016.
- [50] C. Y. Nakashima, S. de Oliveira Jr, and E. F. Caetano, “Calculation of pressure drop in narrow rotating annular clearances.” [Online]. Available: <https://revistas.ufpr.br/reterm/article/view/61756>
- [51] I. Idelchik, “Handbook of hydraulic resistance,” *Boca Raton*, 1994. [Online]. Available: <https://www.nrc.gov/docs/ML1220/ML12209A041.pdf>
- [52] “Examining spatial (grid) convergence.” [Online]. Available: <https://www.grc.nasa.gov/www/wind/valid/tutorial/spatconv.html>
- [53] “Body temperature norms: Medlineplus medical encyclopedia.” [Online]. Available: <https://medlineplus.gov/ency/article/001982.htm>
- [54] “Species specific information: Mouse.” [Online]. Available: <https://web.jhu.edu/animalcare/procedures/mouse.html>
- [55] M. J. Simon and J. J. Iliff, “Regulation of cerebrospinal fluid (CSF) flow in neurodegenerative, neurovascular and neuroinflammatory disease,” *Biochimica et Biophysica Acta - Molecular Basis of Disease*, vol. 1862, no. 3, pp. 442–451, 2016.
- [56] K. Oshio, H. Watanabe, Y. Song, A. S. Verkman, and G. T. Manley, “Reduced cerebrospinal fluid production and intracranial pressure in mice lacking choroid plexus water channel Aquaporin-1,” *The FASEB Journal*, vol. 19, no. 1, pp. 76–78, 2005.
- [57] E. Fransen, R. D’Hooge, G. Van Camp, M. Verhoye, J. Sijbers, E. Reyniers, P. Soriano, H. Kamiguchi, R. Willemsen, S. K. Koekkoek, C. I. De Zeeuw, P. P. De Deyn, A. Van Der Linden, V. Lemmon, R. F. Kooy, and P. J. Willems, “L1 knockout mice show dilated

- ventricles, vermis hypoplasia and impaired exploration patterns,” *Human Molecular Genetics*, vol. 7, no. 6, pp. 999–1009, 1998.
- [58] E. K. Lindstrøm, G. Ringstad, K. A. Mardal, and P. K. Eide, “Cerebrospinal fluid volumetric net flow rate and direction in idiopathic normal pressure hydrocephalus,” *NeuroImage: Clinical*, vol. 20, no. August, pp. 731–741, 2018.
- [59] O. Balédent, M. C. C. Henry-Feugeas, and I. Idy-Peretti, “Cerebrospinal fluid dynamics and relation with blood flow: A magnetic resonance study with semiautomated cerebrospinal fluid segmentation,” *Investigative Radiology*, vol. 36, no. 7, pp. 368–377, 2001.
- [60] “Heart rate: What’s normal? - mayo clinic.” [Online]. Available: <https://www.mayoclinic.org/healthy-lifestyle/fitness/expert-answers/heart-rate/faq-20057979>
- [61] “Hydraulic diameter of an ellipse.” [Online]. Available: <https://www.piping-designer.com/index.php/properties/fluid-mechanics/2250-hydraulic-diameter-of-an-ellipse>
- [62] P. M. Janssen, B. J. Biesiadecki, M. T. Ziolo, and J. P. Davis, “The need for speed,” *Circulation Research*, vol. 119, pp. 418–421, 7 2016.
- [63] J. B. Carr, J. H. Thomas, J. Liu, and J. K. Shang, “Peristaltic pumping in thin non-axisymmetric annular tubes,” *Journal of Fluid Mechanics*, vol. 917, 2021.